

Paleoceanography and Paleoclimatology

RESEARCH ARTICLE

10.1029/2019PA003723

Key Points:

- High-resolution LA-ICP-MS profiles reveal strong diurnal cyclicality in rudist shell
- Dominance of day-night cycle suggests photosymbiosis in the rudist species *Torreites sanchezi*
- Length of annual and daily cycle is used to constrain Campanian Earth-Moon distance

Correspondence to:

N. J. de Winter,
niels.de.winter@vub.be

Citation:

de Winter, N. J., Goderis, S., Van Malderen, S. J. M., Sinnesael, M., Vansteenberge, S., Snoeck, C., et al (2020). Subdaily-scale chemical variability in a *Torreites sanchezi* rudist shell: Implications for rudist paleobiology and the Cretaceous day-night cycle. *Paleoceanography and Paleoclimatology*, 35, e2019PA003723. <https://doi.org/10.1029/2019PA003723>

Received 10 JUL 2019

Accepted 9 JAN 2020

Accepted article online 5 FEB 2020

Subdaily-Scale Chemical Variability in a *Torreites Sanchezi* Rudist Shell: Implications for Rudist Paleobiology and the Cretaceous Day-Night Cycle

Niels J. de Winter¹ , Steven Goderis¹ , Stijn J.M. Van Malderen², Matthias Sinnesael^{1,4} , Stef Vansteenberge¹, Christophe Snoeck^{1,3}, Joke Belza², Frank Vanhaecke², and Philippe Claeys¹ 

¹Analytical, Environmental and Geochemistry Research Group, Vrije Universiteit Brussel, Brussels, Belgium, ²Atomic and Mass Spectrometry Research Unit, Department of Chemistry, Ghent University, Ghent, Belgium, ³Laboratoire G-Time, Département Géosciences, Environnement et Société, Université Libre de Bruxelles, Brussels, Belgium, ⁴Department of Geology, Ghent University, Ghent, Belgium

Abstract This study presents subdaily resolved chemical records through fossil mollusk shell calcite. Trace element profiles resolve periodic variability across ~40-μm-thin daily growth laminae in a Campanian *Torreites sanchezi* rudist bivalve. These high-resolution records are combined with seasonally resolved stable isotope and trace element records that allow shell-chemical variability to be discussed on both seasonal and daily scale. A combination of layer counting, spectral analysis of chemical cyclicality and chemical layer counting shows that the rudist precipitated 372 daily laminae per year, demonstrating that length of day has increased since the Late Cretaceous, as predicted by astronomical models. This new approach to determine the length of a solar day in geologic history through multiproxy chemical records at subdaily resolution yields considerably more control on the uncertainty of this estimate. Daily chemical variability exceeds seasonal variability in our records, and cannot be explained by diurnal temperature changes. Instead, we postulate that rudist shell chemistry is driven on a daily scale by changes in light intensity. These results together with those of stable isotope analyses provide strong evidence that *Torreites* rudists had photosymbionts. Bivalve shell calcite generally preserves well. Therefore, this study paves the way for daily-scale reconstructions of paleoenvironment and sunlight intensity on geologic time scales from bivalve shells, potentially allowing researchers to bridge the gap between climate and weather reconstructions. Such reconstructions improve shell chronologies, document environmental change in warm ecosystems, and widen our understanding of the magnitude of short-term changes during greenhouse climates.

1. Introduction

Both proxy-based paleoclimate reconstructions and climate models characterize the Campanian (83.6 ± 0.5 to 72.1 ± 0.2 Ma; Gradstein et al., 2012) as a warm stage with large fluctuations in climate and sea level (Friedrich et al., 2012; Huber et al., 2002; Pearson et al., 2001). Campanian global mean annual surface temperatures are estimated to have been 2–4 °C warmer than today, with a reduced equator-to-pole temperature gradient (Amiot et al., 2004; Friedrich et al., 2012; Huber et al., 2002). Warm intervals such as the Campanian provide important insights into processes of climate and environmental change that operate during periods with elevated atmospheric CO₂ concentrations (>500 ppm in the Campanian; Gao et al., 2015), such as those predicted for the end of the twenty-first century (Meehl et al., 2007; Price et al., 2013). Most deep-time (pre-Quaternary) climate reconstructions have so far focused on long-term changes in climate and environment on orbital to tectonic time scales (10^3 – 10^8 years; Zachos et al., 2001; Veizer & Prokoph, 2015). However, crucial information can be obtained from the still poorly understood changes on a shorter, human (subannual to decadal) time scale. Combined with long-term climate records, such high-resolution, “snapshot” reconstructions improve current understanding of the dynamics of greenhouse climates and the effect of rapid climate change on the environment. Furthermore, the combination of low- and high-resolution data allows us to study the full spectrum of continuum climate variability and bridge the gap between long- and short-term changes in climate (Huybers & Curry, 2006).

Not only is the study of subdaily resolved records important for understanding environmental change at even higher (daily) temporal resolution, it also enables more accurate estimations of the length of astronomical cycles (e.g., diurnal, tidal, and annual; Bills & Ray, 1999; Williams, 2000). When applied on fossil bioarchives, these observations shed light on the evolution of the Earth-Moon system on geological time scales (Williams, 2000). This information helps to improve constraints on geologic dating through cyclostratigraphy and yields boundary conditions for astronomical models (Berger et al., 1989; Laskar et al., 2004; Meyers & Malinverno, 2018).

Accurately dated and well-preserved hard tissues (e.g., fossil mollusk shells, corals, and biapatites) are valuable archives of subannual to multidecadal paleoenvironmental change (Butler et al., 2013; Fricke et al., 1998; Gothmann et al., 2015; Steuber, 1996). Bivalve shells have proven to be especially useful for reconstructing paleoseasonality and decadal climate variability (e.g., Schöne et al., 2005; Steuber et al., 2005; Watanabe et al., 2004). Indeed, shells of many bivalve species record daily growth increments, especially during the first years of growth (e.g., Pannella, 1972; Schöne, Fiebig, et al., 2005; Warter & Müller, 2017). Hippuritid rudist bivalves (Hippuritidae, Gray 1848) are of special interest for climate reconstructions in the Late Cretaceous, because of their abundance in the fossil record and because their comparatively thick, diagenetically resistant low-Mg calcite (LMC) outer shell layers serve as reliable archives for shallow marine chemistry (Al-Aasm & Veizer, 1986a, 1986b; Steuber, 1996). Since the rudists became extinct at the Cretaceous-Paleogene boundary (Steuber et al., 2002), no close living relatives are available for comparison. As a result, even though rudist taxa have featured in several sclerochronology and geochemistry studies (e.g., Al-Aasm & Veizer, 1986a, 1986b; Gili et al., 1995; Gili & Götz, 2018; Huck & Heimhofer, 2015; Ross & Skelton, 1993; Skelton, 2018; Steuber, 1996, 1999; Steuber et al., 2005), several aspects of their paleobiology remain uncertain. This uncertainty limits the potential of rudist shells as geochemical archives for climate and environmental change during the Cretaceous. One of the most important unresolved hypotheses is whether (some species of) rudists had photosymbionts (Skelton & Wright, 1987; Steuber, 1999; Vermeij, 2013; Vogel, 1975), much like modern scleractinian corals and tridacnid bivalves, which have somewhat similar habitats and life modes. Previous evidence for photosymbiosis in rudists (most notably in species of *Torreites*) include morphological adaptations in the shell such as cavities that could harbor symbionts or promote exchange of chemicals (Skelton, 2018), extensions of the commissure that would support the hypothesized symbiont-bearing mantle (Vermeij, 2013), much like in modern symbiont-bearing tridacnids (Yonge, 1936), envelopment of the upper valve by the symbiont-bearing mantle (Seilacher, 1998; Skelton & Wright, 1987), and exceptionally large shell sizes (e.g., Gili & Götz, 2018; Vermeij, 2013). The presence of photosymbionts would strongly influence the interpretation of geochemical records from rudist shells (e.g., McConnaughey & Gillikin, 2008).

Stable oxygen isotope ratios ($\delta^{18}\text{O}$) are often used in bivalve studies because they record calcification temperature and the oxygen isotope composition of the seawater, the latter of which is strongly linked to salinity (Jones, 1983; Schöne, Fiebig, et al., 2005). Combining $\delta^{18}\text{O}$ records with additional chemical proxies, such as carbon isotope and trace element ratios, in a multiproxy approach makes it possible to discriminate physiological from environmental processes affecting shell chemistry, which leads to more accurate climate reconstructions from bivalve shells (de Winter et al., 2017; Elliot et al., 2009; Schöne et al., 2011). Yet uncertainties persist regarding the exact mechanisms of trace element (e.g., Li, Mg, Sr, and Ba) uptake into bivalve shells, and how environmental conditions influence their incorporation (Füllenbach et al., 2015; Schöne et al., 2011; Weiner & Dove, 2003). Changes in growth rate and vital effects, such as active discrimination against trace elements during Ca^{2+} pumping to the calcification site, heavily influence conventional (e.g., Mg/Ca, Sr/Ca) trace element ratios (Montagna et al., 2014; Weiner & Dove, 2003). This has led to the application of new trace element proxies in sclerochronological studies, such as Mg/Li and Sr/Li, which are less affected by these vital effects (Füllenbach et al., 2015; Montagna et al., 2014).

Recent advances in analytical techniques enable the measurement of trace element ratios at high spatial resolution, equal to or less than 10 μm , a scale at which daily growth increments are recognized in bivalve shells (Sano et al., 2012; Spero et al., 2015; Warter & Müller, 2017). For the first time, the study of shell chemistry at the level of subdaily fluctuations becomes possible, allowing researchers to study the effect of the diurnal light and temperature cycle on shell chemistry (Sano et al., 2012; Warter et al., 2018).

The present study leverages recent improvements in laser ablation-inductively coupled plasma-mass spectrometry (LA-ICP-MS) to perform ultrahigh-resolution (10 μm) elemental profiling through fossil

bivalve shell calcite. This method resolves changes in Mg/Ca, Sr/Ca, Mg/Li, and Sr/Li ratios across thin ($\sim 40 \mu\text{m}$) daily growth laminae in a Campanian *Torreites sanchezi* rudist (Bivalvia: Hippuritidae, Douvillé 1927) from the tropical Saiwan area in present-day Oman ($20^{\circ}40'41.52''\text{N}$, $57^{\circ}35'27.14''\text{E}$; paleolatitude of 5°S). A novel point-by-point analysis (point-by-point-LA-ICP-MS) approach is combined with line-scanning LA-ICP-MS and micro-X-ray Fluorescence (μXRF) profiles as well as stable isotope ($\delta^{18}\text{O}$ and $\delta^{13}\text{C}$) analyses in the same specimen to compare chemical variations on both seasonal and diurnal time scales.

2. Materials and Methods

2.1. Sample Acquisition

The fossilized shell of a complete specimen of *T. sanchezi* was acquired from the Natural History Museum of Maastricht with help of Dr. John Jagt. The specimen was collected in situ from a well-preserved *Vaccinites*-dominated rudist biostrome in the Samhan formation in the Saiwan area in the Sultanate of Oman ($20^{\circ}40'41.52''\text{N}$, $57^{\circ}35'27.14''\text{E}$). The specimen originates from biostrome unit 2 in Philip and Platel (1995) which is located in Unit VI in profile 1 described in Schumann (1995). The Samhan formation is described by Platel et al. (1994) as a shallow marine carbonate platform succession and was dated to be late Campanian in age by Kennedy et al. (2000) based on a revision of the ammonite biostratigraphy of the formation. Two parallel longitudinal cross sections (shown in Figures 1a and 1e, respectively) were cut from the shell and polished with progressively fine grained sandpaper (up to P4000, or $4.5 \mu\text{m}$) and finished with $1\text{-}\mu\text{m}$ grain diameter diamond paste. Sections were color scanned at 6,400 dpi ($\sim 4 \mu\text{m}$) using an Epson Perfection 2,450 high-resolution flatbed color scanner (Epson Corp., Suwa, Nagano, Japan), and thin sections were prepared for microscopic analysis by TS Labs and Geoservice (Cascina, Italy; details in Appendix 1 and Figure S13). (For Appendix and supporting information, see link provided in the Data Availability Statement section.)

2.2. Micro-XRF

Micro X-ray Fluorescence analysis was carried out using a Bruker M4 Tornado energy-dispersive μXRF system (Bruker nano GmbH, Berlin, Germany) at the AMGC research group of the Vrije Universiteit Brussel (Brussels, Belgium). Details on the XRF setup can be found in de Winter and Claeys (2016) and in Appendix 1. Micro-XRF scanning allowed the measurement of semiquantitative, $50\text{-}\mu\text{m}$ -resolution elemental maps of the entire shell surface using a two-dimensional sampling grid and reduced integration time per pixel. Shell preservation was assessed based on XRF maps of strontium (Sr), manganese (Mn), and iron (Fe), thin section microscopy and visual observation of shell structure (see Figure S1; de Winter, Goderis, et al., 2017).

Quantitative, point-by-point line scans were measured in growth direction through the well-preserved LMC outer shell layer at a sampling interval of $25 \mu\text{m}$. This sampling density resolves seasonal- and tidal-scale patterns, but is insufficient for resolving subdaily variability. To produce quantitative XRF spectra, the integration time of each point measurement in these line scans was increased to 60 s until the Time of Stable Reproducibility and Time of Stable Accuracy were reached (de Winter et al., 2017). This measurement strategy achieves the ideal compromise between increased measurement time (improving signal/noise ratio and reducing reproducibility errors) and increased sample size (allowing duplicate analyses and improving sampling density). Spectra were quantified using the Bruker Esprit software calibrated using the matrix-matched BAS-CRM393 limestone standard (Bureau of Analyzed samples, Middlesbrough, UK), after which individual measurements were calibrated offline using seven matrix-matched international certified reference materials (CCH1, COQ1, CRM393, CRM512, CRM513, ECRM782, and SRM1d; see Appendix 1 for details), which were treated as samples. Untreated trace element results are reported in Data S1 in the supporting information.

2.3. Stable Isotope Analyses

A total of 310 small ($\sim 100 \mu\text{g}$) aliquots of calcite were micromilled at $500\text{-}\mu\text{m}$ intervals (seasonally resolved) along a transect in growth direction through the well-preserved LMC shell layer of *T. sanchezi*. Stable carbon ($\delta^{13}\text{C}$) and oxygen ($\delta^{18}\text{O}$) isotope composition of these samples was determined using a NuPerspective Isotope Ratio Mass Spectrometer coupled to a NuCarb carbonate preparation device (Nu Instruments,

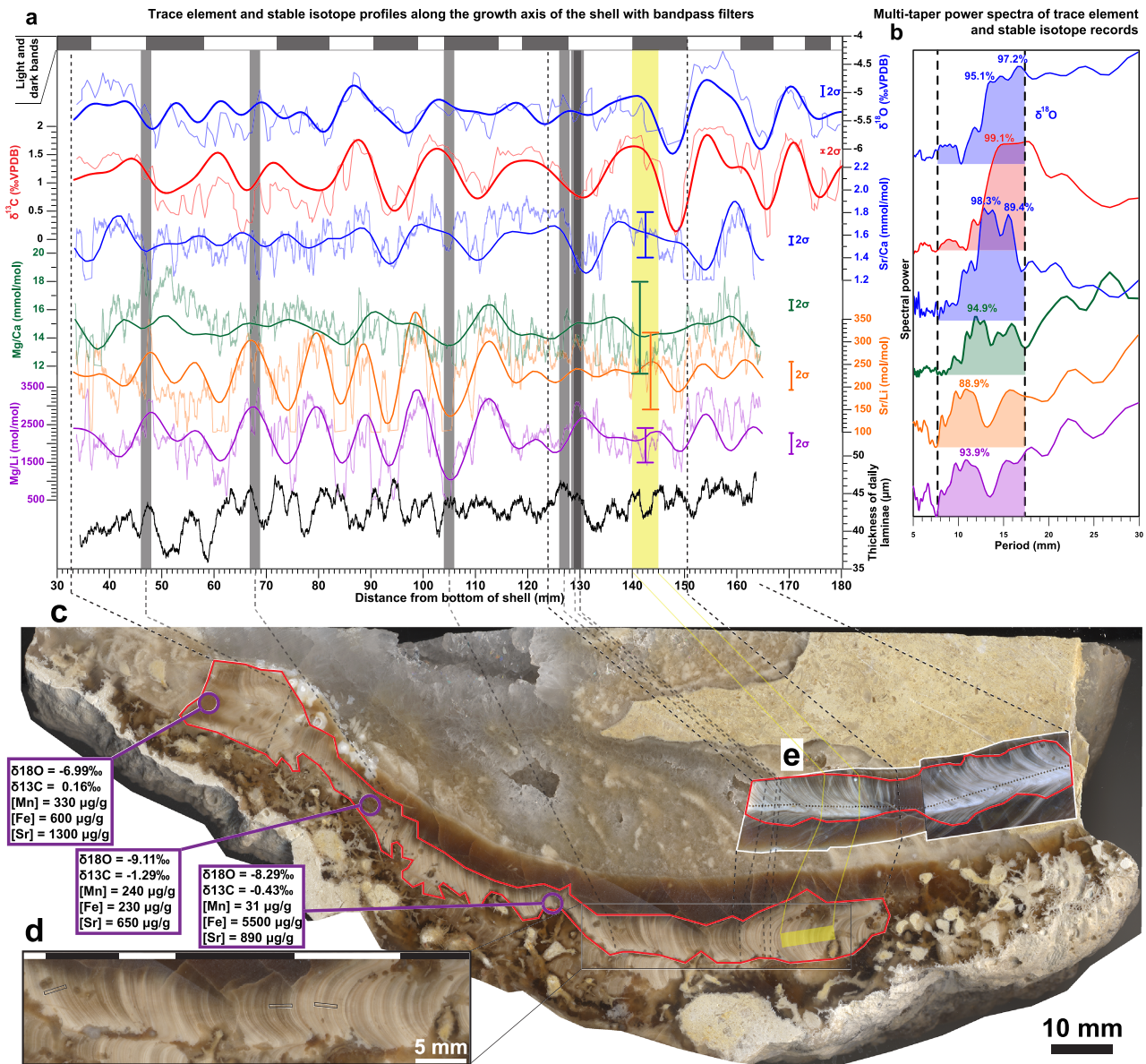


Figure 1. Trace element and stable isotope profiles along the full length of the shell. (a) Records of (from top to bottom) light-dark alternations, $\delta^{18}\text{O}$, $\delta^{13}\text{C}$ Sr/Ca, Mg/Ca, Sr/Li, Mg/Li, and width of daily laminae in *T. sanchezi*. Thin lines illustrate measurements and bold lines represent extracted seasonality (Appendix 1). Grey vertical bars mark positions of point-by-point-LA-ICP-MS profiles (Figure 4), while the yellow bar marks the interval plotted in detail in Figure 2 (close-up) and Figure 3 (plot of the high-resolution record). Capped vertical lines within the yellow area highlight the extent of diurnal variability in trace element records. Purple circles and connected boxes display measurements of diagenetically altered parts of the shell, typically characterized by low values isotopic values ($\delta^{18}\text{O} < -6\text{‰}$; $\delta^{13}\text{C} < 0\text{‰}$), low Sr concentrations ($< 1,000 \mu\text{g/g}$), and high concentrations of Mn and/or Fe ($> 100 \mu\text{g/g}$). (b) Result of spectral analysis (MTM) with focus on the significant peaks at periods that represent annual cyclicity in the proxy records. Percentages indicate statistical significance relative to white noise calculated via an autoregressive model (see Appendix 1). (c) Color scan of longitudinal cross section through the *T. sanchezi* shell. Well-preserved LMC in the outer shell layer is highlighted in red. (d) Close-up of the outer shell layer showing bands of thin laminae with seasonal dark and light shell layers. Black rectangles highlight locations of point-by-point-LA-ICP-MS transects. (e) Insert showing a polished section of well-preserved shell material that is located at the exact location plotted in the figure, but in a parallel cross section through the shell located roughly 10 mm below (in direction perpendicular to the page) the cross section depicted in the remainder of the figure. This section was analyzed to avoid altered parts of the shell on the top part (right side in this image) of the shell in the cross section shown in Figure 1b. Dashed lines are isochrons.

UK). Analytical uncertainty was determined from duplicate sample measurements and repeated analyses on the in-house MAR carbonate standard (68 replicates), which was calibrated to the international NBS-19 stable isotope standard (Friedman et al., 1982), and the IA-603 reference material of the International

Atomic Energy Agency (Vienna, AU; 37 replicates). The combined standard deviation (1σ) based on these measurements was determined to be 0.05‰ and 0.07‰ for $\delta^{13}\text{C}$ and $\delta^{18}\text{O}$ measurements, respectively. Stable isotope results are reported in per mille relative to the Vienna Pee Dee Belemnite standard (‰ VPDB). Untreated stable isotope results are reported in Data S1.

2.4. LA-ICP-MS Analyses

LA-ICP-MS measurements were carried out at the A&MS research unit of the Department of Chemistry of Ghent University (Ghent, Belgium) using an Analyte G2 ArF*excimer-based laser ablation system (Teledyne Photon Machines, Bozeman, USA) coupled to a Thermo X Series 2 (for point-by-point-LA-ICP-MS; Thermo Fisher Scientific, Bremen, Germany) or an Agilent 7900 (for LA-ICP-MS; Agilent, Santa Clara, USA) quadrupole-based ICP-MS unit. Two types of LA-ICP-MS measurements were applied, continuous line scans and high-resolution point-by-point transects. LA-ICP-MS line scans were measured along the entire shell length of *T. sanchezi* by continuous line scanning using a circular 10- μm spot (subdaily resolution). Six 2-mm-long point-by-point-LA-ICP-MS profiles were measured at 10- μm (subdaily) resolution by point-by-point ablation using a 150 \times 10- μm rectangular spot positioned parallel to fine growth laminae visible in the shell. More details on the LA-ICP-MS measurement setup are given in Appendix 1. LA-ICP-MS results were calibrated using repeated measurements of United States Geological Survey (USGS) BCR-2G, USGS BHVO-2G, USGS GSD-1G, and USGS-GSE-1G and National Institute of Standards and Technology SRM610 and National Institute of Standards and Technology SRM612 certified natural and synthetic glass reference materials. Uncertainties on LA-ICP-MS measurements are given in Table S2. All untreated LA-ICP-MS data used in this study are presented in Data S1. Detailed plots of high-resolution, subdaily resolved, point-by-point LA-ICP-MS analyses are given in Figures S7–S12.

2.5. Microscopy

Thin sections were prepared from well-preserved parts of the outer shell layer. Light microscopy was carried out at 250X and 4,000X magnification on uncovered thin sections using a Nikon Optiphot 2 POL transmitted light microscope (Nikon Corp., Tokyo, Japan) and on polished shell cross sections using a Meiji EM2-13TR reflected light stereomicroscope. Detailed images of the shell structure and the fine lamination present in well-preserved parts of the shell were recorded using regular and polarized light sources. A composite of 250X magnification images of the fine lamination visible in the shell and examples of images showing the fine lamination and diagenetic features in the shell are given in Figures 2 and S13. See Appendix 1 for details on the microscopic setup.

2.6. Age Model

An age model was created for the *T. sanchezi* shell using a MATLAB® modeling routine that simulates the stable isotope record in a shell by iteratively fitting growth rate and temperature sinusoids to the data to arrive at a subannual resolved growth model (Judd et al., 2018). This routine was adapted from Judd et al. (2018) to allow modeling of calcitic rather than aragonitic bivalve shells (modified MATLAB routine given in Data S7) and applied to the carbon isotope curve of the *T. sanchezi* shell, which exhibits the clearest seasonal pattern. The main adaptation of the growth model routine consisted of the implementation of the equation by Kim and O'Neil (1997) which describes equilibrium isotopic fractionation between calcite and water rather than the aragonite-water equation originally used by Judd et al. (2018). The model takes isotope data and positions of the onset of annual cycles in the record as input. It then iteratively fits a combination of sinusoids of growth rate and temperature to every consecutive year in the record, after which the age models can be stitched together to produce a single continuous age sequence for the full isotopic record. Results of this age model are given in Data S6 and plotted in Figure 3. As a result, the model produces an age in days of the year relative to the seasonal cycle for each stable isotope measurement. These modeled ages in turn allow the determination of growth rates (in mm/day) in the direction of measurement for each day of growth.

2.7. Signal Processing

Signal processing was carried out on long records of Mg/Ca, Mg/Li, Sr/Ca, Sr/Li, $\delta^{18}\text{O}$, and $\delta^{13}\text{C}$ as well as on the high-resolution records of Mg/Ca, Mg/Li, Sr/Ca, and Sr/Li using the Multitaper Method (MTM; Thomson, 1982) in the “astrochron” package built in the open-source computational software package R (Meyers, 2014; R Development Core Team, 2008). Confidence estimates relative to white noise were made

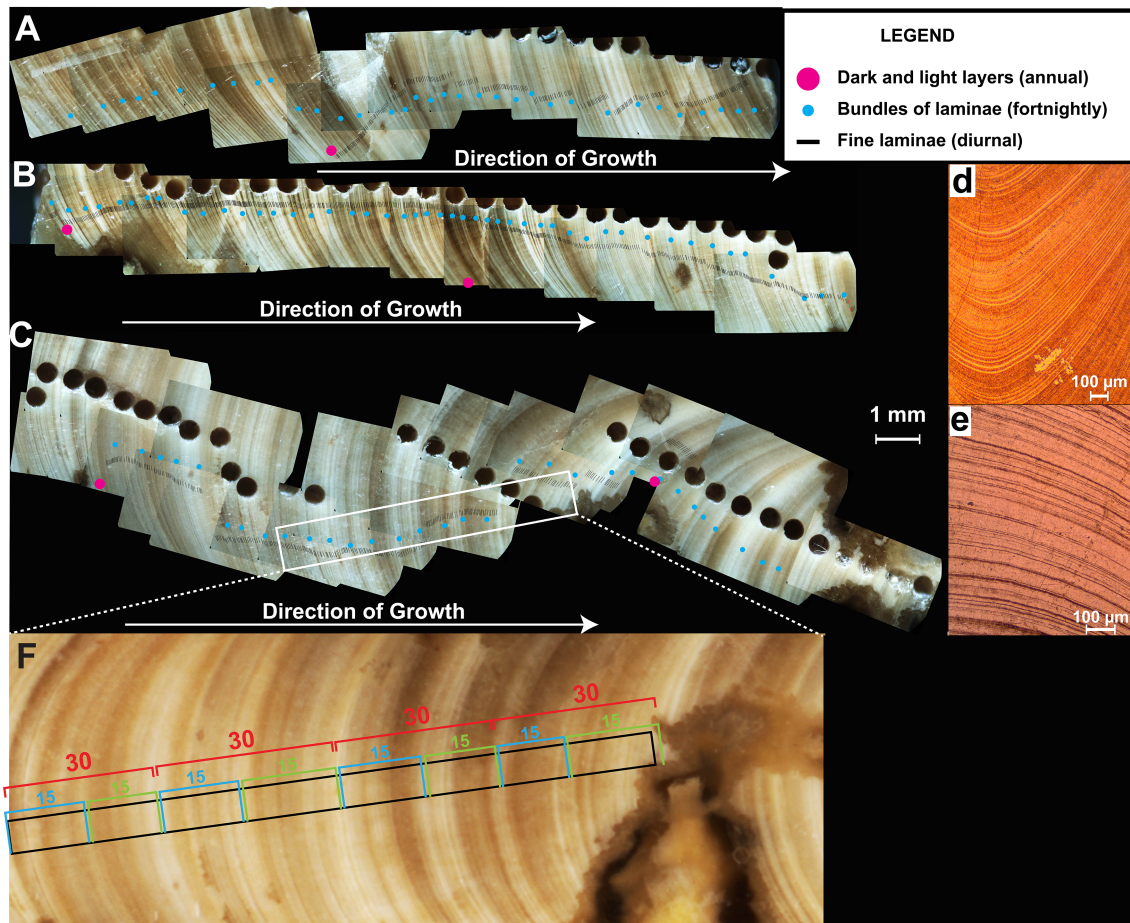


Figure 2. Microscopic observations of shell laminae and bundling. (a–c) Composite of microscope images of a part of the outer shell surface of *T. sanchezi* which shows well-expressed seasonal cyclicity in calcite layers (Figure 1d). Sections shown in A, B, and C are shown in order of shell age, with the rightmost parts of A and B matching the leftmost parts of B and C, respectively (growth from left to right). Distances between red dots represent one year of growth (based on stable oxygen isotope records). Distances between green dots represent 0.6-mm-long bundles of laminae associated with the fortnightly tidal cycle. Individual fine daily laminae are indicated with black lines. These are counted to obtain independent evidence for the number of days per year and the length of a daily cycle recorded in the shell of *T. sanchezi* (see section 4). (d) Thin section micrograph of a dark part of LMC outer shell layer showing ~40-μm-thick laminae with prominent dark calcite bands. (e) Thin section micrograph of a lighter part of LMC outer shell layer showing ~40-μm-thick laminae with prominent lighter calcite bands. Note the difference in scale with (e). (f) Close-up of a section of the shell indicated by the white box in Figure 2c. Green and blue brackets highlight the fortnightly tidal bundling clearly visible in this section, while larger red bundles show the monthly (28 days) bundling. Trace element records from the same exact section are shown in Figure 3.

for all investigated frequencies using an autoregressive noise model. Significant frequencies of annual and daily cyclicity were filtered out of the long and high-resolution records, respectively, by selecting frequencies with the highest confidence levels (>90%; see Figures 1b and 5e and Appendix 1). A tapered cosine (Tukey) band-pass window was applied to filter out the selected frequencies, after which filtered time series were plotted together with analysis results (Figures 1a and 4; see Meyers, 2014).

Stacks of daily and annual cycles were constructed by identifying the maxima, minima, and crossover points of band-pass filters of statistically significant periodicities associated with daily laminae. Proxy records were aligned to the cyclicity of band-pass filters based on the position of these tie points. The location of each measurement relative to the extracted cycle was used to plot all measurements on one axis relative to the phase of the cycle and create daily and annual stacks of proxy records. Details on the signal processing and stacking procedure are given in Appendix 1, and R-scripts applied for data treatment are presented in Data S2. Results of band-pass filtering, stacking, and multitaper method spectral analysis are documented in Data S3–S5, respectively.

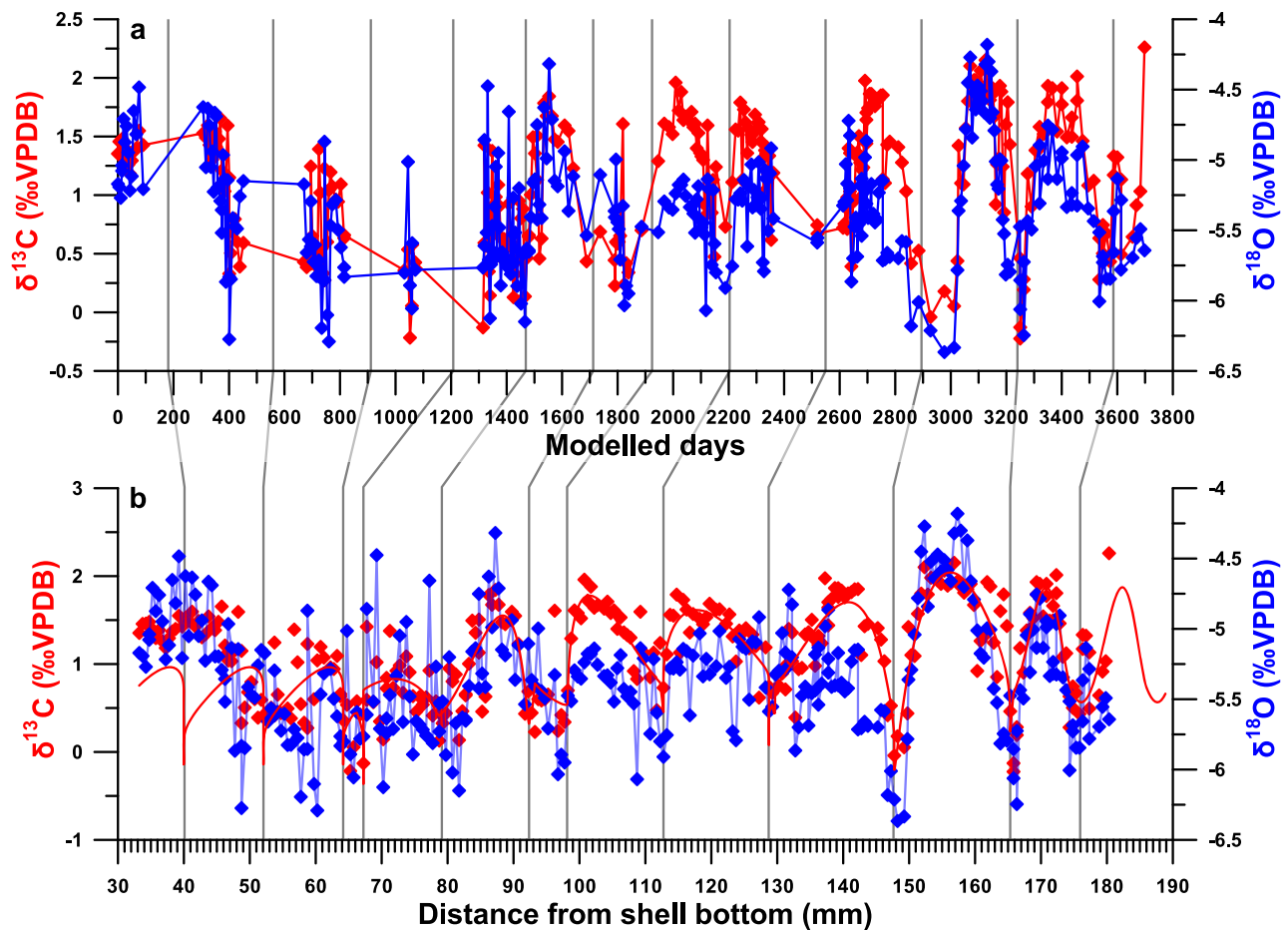


Figure 3. Result of $\delta^{18}\text{O}$ and $\delta^{13}\text{C}$ measurements plotted (a) against modeled age (in days, after age modeling based on the seasonal cyclicity observed in the records using model by Judd et al., 2018) and (b) against distance along the shell record (in mm from shell bottom, before age modeling). Vertical lines connecting the two panels represent the same location along the record. The full, curved lines indicate the modeled stable isotope values, while symbols indicate measurements.

2.8. Calculations of Length of Day and Earth-Moon Distance

Based on subdaily resolved Mg/Ca, Mg/Li, Sr/Ca, and Sr/Li records and the microscopic observations of laminae in the shell, and the assumption that these laminae represent (solar) days (see section 4), the number of days in the late Campanian year with associated uncertainty was estimated using three independent methods.

The first estimate of the number of days per year (**cycle length**) was made by dividing the length of the annual cycle, in micrometer shell length along the record extracted from the long trace element and stable isotope records (Figure 1a) using the identification of significant peaks from the MTM spectrum (Figure 1b), by the length of the daily cycle extracted similarly from the power spectra of high-resolution records. The uncertainties of these two estimates were calculated as the standard deviation of variability between cycle length estimates from the records ($N = 6$ for the annual cycle in seasonally resolved Mg/Ca, Mg/Li, Sr/Ca, Sr/Li, $\delta^{18}\text{O}$, and $\delta^{13}\text{C}$ records; $N = 4$ for the daily cycle in subdaily resolved Mg/Ca, Mg/Li, Sr/Ca, Sr/Li records), and propagated through the calculation.

The second estimate the number of days per year (**visual layer counting**) was made from counting the number of daily laminae within one year of growth from the composite of microscopic images of the shell (reflected light microscopy in Figure 2 and transmitted thin section microscopy in Figure S13). The uncertainty of this estimate was calculated as the standard deviation of variability between counting results

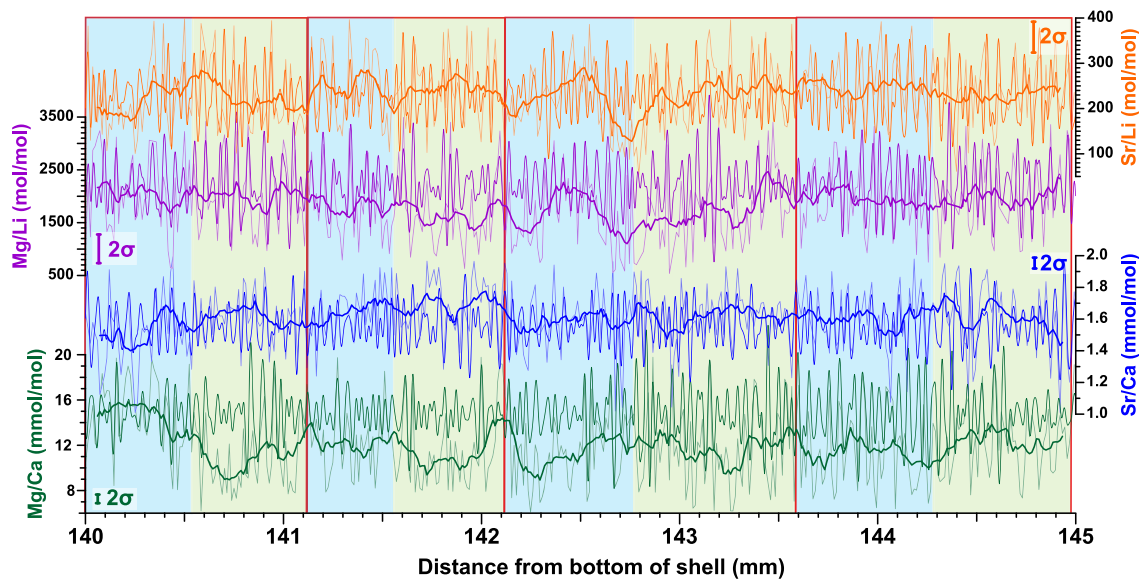


Figure 4. Detail of high-resolution trace element record. (a) High-resolution (10 μm) LA-ICP-MS records of Mg/Ca, Sr/Ca, Mg/Li, and Sr/Li measured perpendicular to the orientation of $\sim 40\text{-}\mu\text{m}$ laminae in *T. sanchezi* shell (yellow bar in Figure 1, close-up shown in Figure 2f). Shaded lines represent measurements while thin lines designate band-pass filters of dominant $\sim 40\text{-}\mu\text{m}$ periodicities and bold lines represent moving averages through records indicating millimeter-scale variability. Light blue, green, and red boxes indicate bundles of ~ 15 and ~ 30 laminae which correspond to the brackets in Figure 2f.

from different growth years and on different microscopic images (transmitted and reflected light). These first two estimates are likely to underestimate the actual number of laminae, because parts of the shell with less distinct (visual or chemical) expression of the daily laminae lead to missing laminae (in the **visual layer counting**) and overestimation of laminae width (in the **cycle length** estimate).

The third estimate the number of days per year (**chemical layer counting**) is unique to this study and uses fixed points (maxima, minima, and crossover points) of cycles extracted from the high-resolution trace element records by band-pass filtering to obtain a record of day-by-day cycle length along the complete nine-year-long record measured in *T. sanchezi* (Figure 1a and section 3). Not only does this estimate allow the number of days per year to be estimated with more confidence ($N = 36$ independent estimates: nine growth years times four trace element records), it also allows one to calculate the part of the record that preserves daily lamination (**%preservation**) for each record and each growth year separately. This is achieved by dividing the number of positively identified laminae multiplied by their average length (yielding the fraction of the record containing well-expressed laminae) by the total length of the growth year (as determined from the spacing of annual growth layers in the microscopy images and seasonality recorded in the stable isotope curve): $\% \text{preservation} = \frac{N_{\text{laminae}} * L_{\text{laminae}}}{L_{\text{year}}}$. The **chemical layer counting** is corrected for each year and record individually by dividing the number of days per year by the fraction of record preserved. The estimates of number of days per year based on **cycle length** and **visual layer counting** (which underestimate the actual number of days; see above) are corrected in the same way (more details in Data S9).

The length of a Campanian day is calculated by dividing the length of a year in seconds (which remained constant over geological time; Williams, 2000) by the number of days per year. The Earth-Moon distance can be calculated via the assumption that the total inertia and energy of the Earth-Moon system remains constant over time (Lowrie, 2007). This energy can be summed up as the rotational energy of the Earth and Moon around their axes and the energy of rotation of the Moon around the Earth. The rotational energy of the Moon around its axis is several orders of magnitude smaller than the other two components ($\sim 10^{32}$ versus $\sim 10^{37}$ J; see Appendix 1) and may therefore be neglected in this calculation (Lowrie, 2007). As a result, energy lost from Earth's rotation (leading to slower rotation and longer days) is transferred almost completely to the energy of the Moon's rotation around Earth (increasing the Earth-Moon distance) by means of

Table 1

List of records of cycle counting results from records of trace element proxies (molar ratios of Mg/Ca, Mg/Li, Sr/Ca, and Sr/Li), showing the significance of peaks of daily (for high-resolution records) and annual (for longer lower resolution records) cyclicity found by spectral analysis and white noise estimation. In addition, the expression of the cyclicity in color, the length of the period, and the number of cycles in the record are reported.

Proxy	Section	Cycle	Position of section (μm from shell bottom)	Expression of seasonal cycle	Peak significance (%)	period (μm)	# of cycles
Mg/Ca (mmol/mol)	I	diurnal	42393 - 44393	light/dark	73.4%	36.58	55
	II	diurnal	66826 - 68826	light	96.8%	39.57	51
	III	diurnal	103939 - 105939	dark	92.5%	34.72	58
	IV	diurnal	126010 - 128010	dark	98.2%	33.78	59
	V	diurnal	128320 - 130320	light	68.6%	37.45	53
	VI	diurnal	128740 - 130740	light	84.6%	39.26	51
	Long record	annual	33240 - 180327		94.9%	13743	8
Mg/Li (mol/mol)	I	diurnal	42393 - 44393	light/dark	94.0%	39.06	51
	II	diurnal	66826 - 68826	light	97.7%	35.59	56
	III	diurnal	103939 - 105939	dark	88.6%	36.01	56
	IV	diurnal	126010 - 128010	dark	95.3%	34.32	58
	V	diurnal	128320 - 130320	light	95.1%	37.04	54
	VI	diurnal	128740 - 130740	light	97.9%	35.88	56
	Long record	annual	33240 - 180327		88.9%	12449	6
Sr/Ca (mmol/mol)	I	diurnal	42393 - 44393	light/dark	77.9%	40.16	50
	II	diurnal	66826 - 68826	light	96.7%	36.28	55
	III	diurnal	103939 - 105939	dark	94.1%	35.09	57
	IV	diurnal	126010 - 128010	dark	89.2%	36.23	55
	V	diurnal	128320 - 130320	light	97.1%	37.31	54
	VI	diurnal	128740 - 130740	light	89.9%	32.43	62
	Long record	annual	33240 - 180327		98.2%	13582	8.5
Sr/Li (mol/mol)	I	diurnal	42393 - 44393	light/dark	81.7%	34.17	59
	II	diurnal	66826 - 68826	light	97.5%	36.36	55
	III	diurnal	103939 - 105939	dark	93.5%	34.35	58
	IV	diurnal	126010 - 128010	dark	96.3%	39.06	51
	V	diurnal	128320 - 130320	light	96.5%	37.31	54
	VI	diurnal	128740 - 130740	light	95.9%	37.92	53
	Long record	annual	33240 - 180327		93.9%	13002	6
$\delta^{13}\text{C}$	Long record	annual	33240 - 180327		99.1%	14471	9
$\delta^{18}\text{O}$	Long record	annual	33240 - 180327		97.2%	12939	9

tidal dissipation (Williams, 2000). Given the constant length of Earth's year, this energy balance allows the Earth-Moon distance to be directly related to the number of days per year (or the ratio between length of day and length of year). The derivation of the formulae used for these calculations (after Lowrie, 2007) is presented in Appendix 1.

3. Results

3.1. Preservation

Microscopy and μXRF mapping (see Figure S1) together with color scans and micrographs (Figure 1c–e; Figure 2) reveal that the interior of *T. sanchezii*'s LMC outer shell layer is exceptionally well-preserved. This is evident from low Mn (typically $<50 \mu\text{g/g}$) and Fe (typically $<100 \mu\text{g/g}$) concentrations and high Sr (typically 1,200–1,400 $\mu\text{g/g}$) concentrations as well as preservation of microscopic ($\sim 40 \mu\text{m}$ wide) growth laminae (Al-Aasm & Veizer, 1986a; de Winter et al., 2017a). At the same time, stable isotope analyses show that these well-preserved parts of the shell are characterized by $\delta^{18}\text{O}$ values fluctuating periodically between -6‰ and -4.5‰ VPDB, which, although relatively low for bivalve calcite, is comparable with records of pristine calcite from this and other rudist species from the Late Cretaceous (Steuber, 1996, 1999; Steuber et al., 2005). Similarly, periodic fluctuations of $\delta^{13}\text{C}$ values between 0.5‰ and 2‰ VPDB are consistent with carbon isotope ratios in other well-preserved fossil bivalve shells (e.g., Batenburg et al., 2011; Steuber, 1996, 1999).

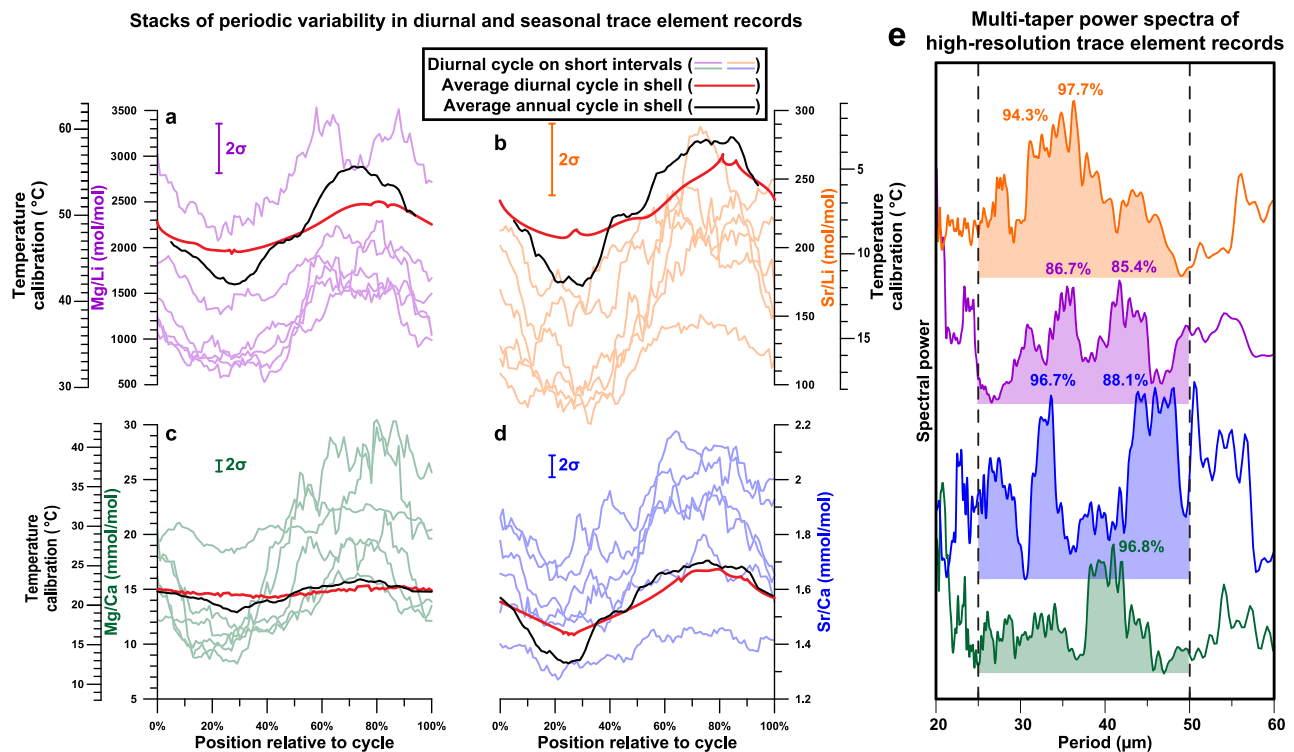


Figure 5. Stacks of seasonal and diurnal variability in trace element records. Stacks of daily (red and shaded lines) and seasonal (dashed black lines) variation in (a) Mg/Li, (b) Sr/Li, (c) Mg/Ca, and (d) Sr/Ca. Positions of point-by-point-LA-ICP-MS sections (shaded lines) are illustrated in Figure 1a. Vertical error bars indicate 2 standard deviations of measurement error. “Temperature calibration” axes show tentative temperature estimates based on calibrations for Mg/Ca (Surge & Lohmann, 2008), Mg/Li (Montagna et al., 2014), and Sr/Li (Füllenbach et al., 2015). (e) Results of spectral analysis (MTM) with focus on the significant peaks at periods that represent daily cyclicity in the proxy records. Percentages indicate statistical significance relative to white noise calculated via an autoregressive model (see Appendix 1).

Comparison of these values with stable isotope and trace element measurements in visually altered parts of the shell (Figure 1a) indicates that these diagenetic parts are characterized by lower stable isotope values ($\delta^{18}\text{O} < -6\text{‰}$; $\delta^{13}\text{C} < 0\text{‰}$), lower Sr concentrations ($[\text{Sr}] < 1,000 \mu\text{g/g}$) and higher concentrations of Mn & Fe ($[\text{Mn}] > 100 \mu\text{g/g}$; $[\text{Fe}] > 250 \mu\text{g/g}$). The trace element and isotopic compositions of well-preserved parts of *T. sanchezi* that exhibit fine laminae resemble compositions of pristine LMC reported in Al-Aasm & Veizer (1986a, 1986b). The geochemical differences between well-preserved and altered shell material described above match the geochemical changes associated with transitions from pristine rudist calcite toward diagenetically altered shell material observed by Al-Aasm & Veizer (1986a, 1986b). This demonstrates that the parts of *T. sanchezi* that were analyzed in this study are indeed well-preserved.

The $\delta^{13}\text{C}$ and $\delta^{18}\text{O}$ records clearly covary, on the seasonal scale as well as on the scale of the aforementioned millimeter-scale fluctuations (see Figure 1a). A cross plot in Figure 6a shows that this correlation is moderate in strength ($R^2 = 0.47$) and highly statistically significant ($p \ll 0.05$). Note that positive correlations between $\delta^{13}\text{C}$ and $\delta^{18}\text{O}$ records have been put forward by previous authors as evidence for disequilibrium fractionation and signs of diagenetic alteration (e.g., Huck & Heimhofer, 2015; McConnaughey, 1989; Steuber, 1999). However, the evidence cited above (see also Figure 1) shows that stable isotope samples originated from the most pristine parts of the *T. sanchezi* outer shell layer, rendering diagenetic alteration unlikely.

Despite this evidence for good preservation, we cannot fully exclude the possibility that some remobilization of specific elements took place between shell laminae on a microscale. Growth lines in bivalves are generally characterized by elevated amounts of organic matter and are therefore susceptible to geochemical alteration (Clark, 1999). Such potential microscale alteration does not significantly change the discussion of daily lamination put forward in this work.

Table 2

Concentrations of Li, Mg, Sr, and Ca measured in six point-by-point-LA-ICP-MS transects measured at different locations in the shell. μ XRF, LA-ICP-MS line scan, and stable isotope analysis results in the long record along the full length of the shell are also given. Molar ratios (Mg/Ca, Mg/Li, Sr/Ca, and Sr/Li) are directly calculated from these measurement results and are given in separate columns. Columns indicate the ranges and amplitude of daily and annual cyclicity as well as the ranges and amplitudes of tentative temperature estimates based on temperature calibrations found in the literature based on the different proxies.

Proxy	Section	Cycle	Position of section (μ m from shell bottom)	Mean value	Range of cycle	Amplitude of cycle	Measurement error (1SD)	Pearson's r	p-value	Temperature range of cycle	T_range
Mg/Ca (mmol/mol)	I	diurnal	42393 - 44393	20.95	11.38 30.32	18.93	± 1.22	0.58	6.50E-19	16.1 42.4	26.3
	II	diurnal	66826 - 68826	13.13	10.70 16.69	5.99		0.62	8.10E-23	15.2 23.5	8.3
	III	diurnal	103939 - 105939	14.62	8.87 22.17	13.30		0.58	1.25E-19	12.6 31.1	18.5
	IV	diurnal	126010 - 128010	13.57	8.21 19.60	11.40		0.62	2.20E-22	11.7 27.5	15.8
	V	diurnal	128320 - 130320	18.74	8.65 30.45	21.80		0.64	1.33E-24	12.3 42.6	30.3
	VI	diurnal	128740 - 130740	20.68	18.29 22.77	4.48		0.44	6.67E-11	25.7 31.9	6.2
	Long record	annual	33240 - 180327	11.35	10.06 12.57	2.51		0.36	<1E-100	14.3 17.8	3.5
Mg/Li (mol/mol)	I	diurnal	42393 - 44393	1210	778 1666	888	± 267	0.58	1.43E-19	29.3 44.9	15.5
	II	diurnal	66826 - 68826	1751	1270 2234	964		0.53	5.07E-16	39.3 50.9	11.5
	III	diurnal	103939 - 105939	1154	528 1894	1366		0.58	3.01E-19	21.4 47.5	26.1
	IV	diurnal	126010 - 128010	1074	577 1779	1202		0.56	1.74E-17	23.2 46.2	23.0
	V	diurnal	128320 - 130320	1384	776 2297	1522		0.62	1.88E-22	29.3 51.4	22.2
	VI	diurnal	128740 - 130740	2779	2076 3535	1459		0.38	2.80E-08	49.4 60.2	10.9
	Long record	annual	33240 - 180327	1414	1034 2362	1329		0.31	<1E-100	35.1 52.0	16.9
Sr/Ca (mmol/mol)	I	diurnal	42393 - 44393	1.74	1.50 1.95	0.45	± 0.11	0.54	2.26E-16		
	II	diurnal	66826 - 68826	1.59	1.45 1.80	0.35		0.54	2.13E-16		
	III	diurnal	103939 - 105939	1.89	1.63 2.18	0.54		0.60	3.36E-21		
	IV	diurnal	126010 - 128010	1.90	1.63 2.13	0.49		0.60	3.42E-21		
	V	diurnal	128320 - 130320	1.71	1.48 1.98	0.51		0.54	2.72E-16		
	VI	diurnal	128740 - 130740	1.39	1.27 1.46	0.19		0.33	2.18E-06		
	Long record	annual	33240 - 180327	1.46	1.22 1.63	0.41		0.57	<1E-100		
Sr/Li (mol/mol)	I	diurnal	42393 - 44393	115	82 151	69	± 30	0.52	5.31E-15	19.2 13.6	5.5
	II	diurnal	66826 - 68826	216	152 288	136		0.62	5.85E-23	13.6 2.6	11.0
	III	diurnal	103939 - 105939	158	71 241	170		0.63	1.76E-23	20.0 6.3	13.7
	IV	diurnal	126010 - 128010	160	80 245	165		0.62	2.55E-22	19.3 6.1	13.3
	V	diurnal	128320 - 130320	147	92 236	144		0.63	1.46E-23	18.4 6.8	11.6
	VI	diurnal	128740 - 130740	187	133 233	100		0.38	2.89E-08	15.1 7.0	8.0
	Long record	annual	33240 - 180327	92	63 133	70		0.29	4.60E-98	20.7 15.1	5.6
d13C	Long record	annual	33240 - 180327	1.13	0.53 1.63	1.10	± 0.03	0.65	3.36E-39		
d18O	Long record	annual	33240 - 180327	-5.36	-5.76 -5.03	0.73	± 0.09	0.59	6.43E-31	43.0 34.0	9.0

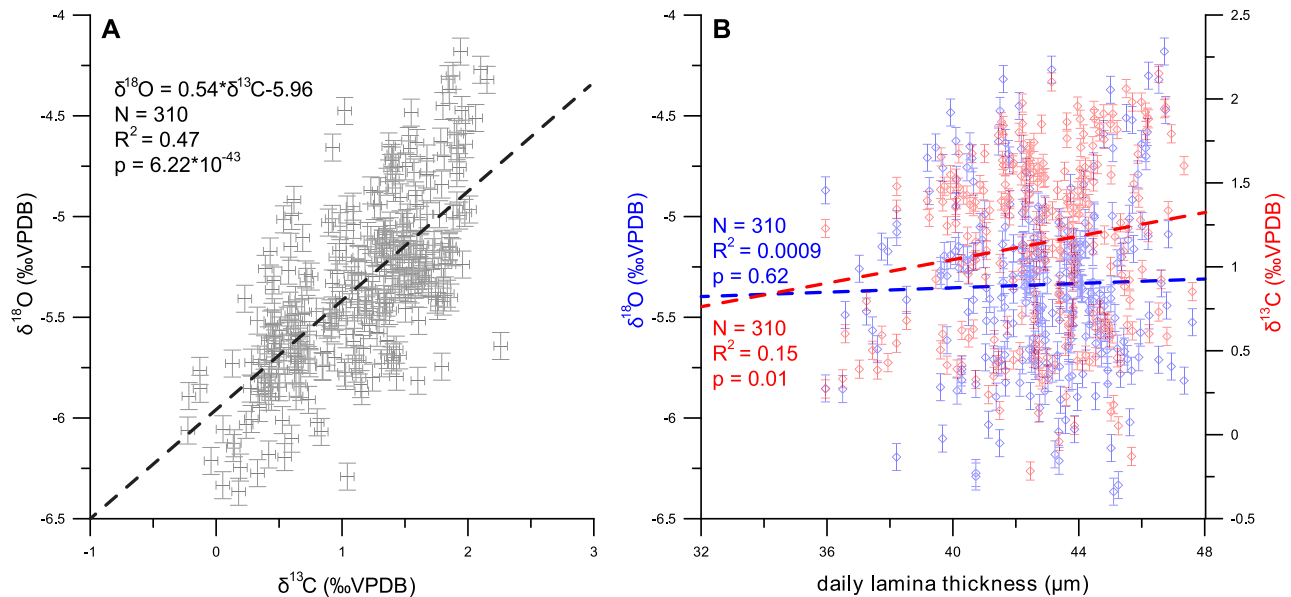


Figure 6. Cross plots showing (a) statistically significant correlation between $\delta^{18}\text{O}$ and $\delta^{13}\text{C}$ in stable isotope profiles through *Torreites sanchezi* low-magnesium calcite outer shell layer (black dotted line shows linear correlation), (b) the clear lack of statistical significance ($p > 0.05$, $R^2 \ll 0.1$; blue dotted line) in the visually apparent correlation between daily lamina thickness and $\delta^{18}\text{O}$ and the weak significant correlation ($p < 0.05$, $R^2 = 0.15$; red dotted line) between lamina thickness and $\delta^{13}\text{C}$.

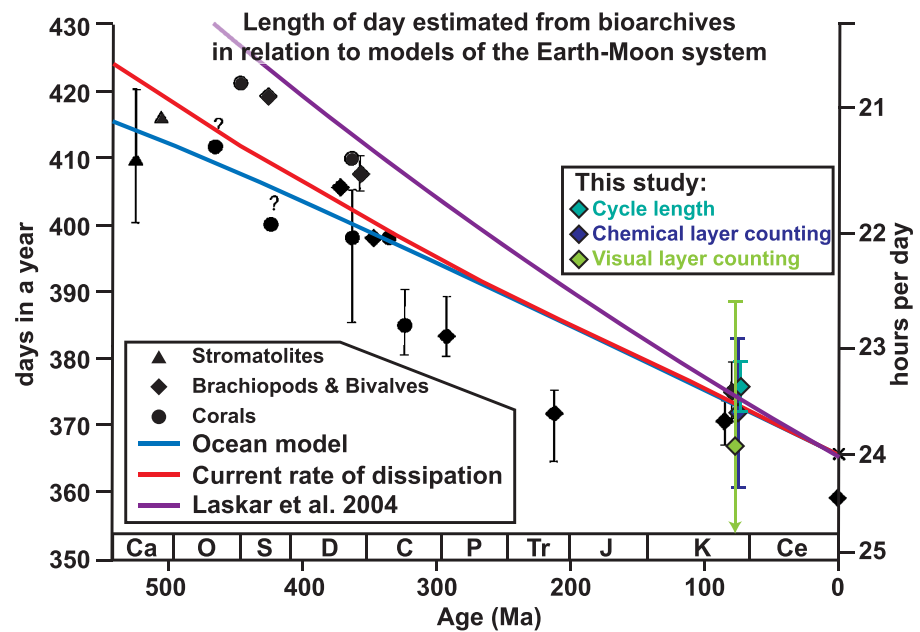


Figure 7. Length of day in the Phanerozoic estimated from bioarchives. Black symbols illustrate estimates from various bioarchives from the literature (compiled by Williams, 2000). Green symbols and error bars (2σ ; offset for illustration purposes only) highlight this study's results. Colored lines show evolution of diurnal and annual cycles according to three models for the Earth-Moon system (Ocean Model after Bills and Ray (1999), Constant Dissipation model after Meyers and Malinverno (2018), and astronomical model after Laskar et al. (2004)).

3.2. Proxy Records

Seasonally resolved geochemical proxy records (Mg/Ca , Sr/Ca , Mg/Li , Sr/Li , $\delta^{18}\text{O}$, and $\delta^{13}\text{C}$) measured in growth direction through the well-preserved part of the shell, and rhythmic alternations of dark and light shell calcite show a statistically significant ($p \leq 0.05$) cyclicity linked to the seasonal cycle with a period of 14.8 ± 0.1 mm. In these alternations, dark bands in the shell correspond with minima in $\delta^{18}\text{O}$ values and vice versa. This relationship between $\delta^{18}\text{O}$ values and the coloration of shell calcite is especially clear in the intervals 30–60, 70–110, and 140–180 mm, where the periodic fluctuations in $\delta^{18}\text{O}$ values are more obvious (see de Winter, Goderis, et al., 2017; Figures 1a–1d, 2, and S3 and Table 1; details in Appendix 1). Annual periodicity in stable isotope records allowed an accurate seasonally resolved shell chronology to be established (following Judd et al., 2018; Appendix 1 and Figure 3; details in section 2). Figure 3 shows how this age model allows conversion of the stable isotope data from the depth to the time domain. The same conversion was applied to the trace element records. As a result, the model shows that a total of 10 growth years are captured in the stable isotope records (the last year starting 176 mm from the shell bottom is not complete), while the shorter (30–160 mm from shell bottom) but higher-resolution trace element records cover only nine growth years (see also Figure 1a). Age modeling using the routine by Judd et al. (2018) is more successful in the last six recorded years, which exhibit clearer seasonal fluctuations than the noisier first four years.

Figure 1 shows that both $\delta^{13}\text{C}$ and $\delta^{18}\text{O}$ records are characterized by small ($0.2\text{--}0.3\text{‰}$) millimeter-scale fluctuations superimposed on the seasonality described above, which cannot completely be subscribed to measurement noise (standard deviation of analytical uncertainty $<0.1\text{‰}$). The same observation is true for trace element records (compare millimeter-scale fluctuations with the size of analytical uncertainties presented in Figure 1a). These smaller-scale fluctuations are most prominent in the first four recorded growth years.

3.3. Timing of Lamina Deposition

Laterally continuous subannual laminae in the shell of *T. sanchezi* are composed of couplets of dark and light layers with a combined thickness of ~ 40 μm (Figures 1c–1e and 2). The relative thickness of these

dark and light layers within a lamina varies and causes the above-mentioned seasonal color variations (see Figures 1a, 1d, 1e, 2, and S3). Laminae are bundled in sets of ~15 and ~30 laminae with an average width of ~0.6 and ~1.2 mm, respectively. These bundles are clearly visible in the microscopic images, high-resolution chemical records, and color scans of well-preserved parts of the shell, and are identified with statistical significance using spectral analysis on color records extracted from the scans ($p < 0.05$; Figures 2, 4, and S3).

The first estimate of the number of laminae deposited by *T. sanchezi* within one year was obtained by dividing the length of the annual by that of the daily cycle, as obtained through frequency analysis, yielded an average of 346 ± 3.3 laminae per year ($\frac{14,800 \pm 100 \mu\text{m}}{42.7 \pm 0.34 \mu\text{m}} = 346 \pm 3.3$ days/year; **cycle length**; see section 2.8). The second estimate, based on **visual layer counting** on both reflected light and transmitted light (thin section) microscopy (see Figures 2 and S13), yields an average of 338 ± 20 laminae per year. As mentioned above (section 2.8), both of these results underestimate the number of laminae deposited per year due to incomplete preservation of the laminae across the entire shell length.

The 10- μm spatial resolution of our LA-ICP-MS profiles resolves strong variations in Mg/Ca, Sr/Ca, Mg/Li, and Sr/Li ratios across laminae in *T. sanchezi* (Figure 4 and Table 1). In addition, six 2-mm-long point-by-point-LA-ICP-MS profiles capture the full amplitude of chemical variability at intervals where these laminae are exceptionally well expressed (Figure 5 and Tables 1 and 2). Overlapping sections demonstrate that these fluctuations are reproducible between profiles and in isochronous parts of the shell (Figure S4). Furthermore, a LA-ICP-MS line-scan record allows the width of fine laminae to be traced through the entire shell (see Figure 1a, Table 1, Appendix 1, and Data S8), and enables counting of the number of laminae per year in four trace element records across nine consecutive years (**chemical layer counting**; see section 2.8 and details in Appendix 1), leading to 36 separate estimates of the amount of days per year (nine growth years recorded in four trace element records). On average, 92% of the LA-ICP-MS data set was of sufficient quality to allow identification of cycles associated with the subannual laminae. After correcting for this incomplete preservation on a record-by-record and year-by-year basis (Data S9), **chemical layer counting** yields an average of 373 ± 12 laminae per year (Appendix S6). Similarly, this measure of preservation can be used to correct the previous two estimates, yielding estimates of 376 ± 3.6 and 367 ± 22 laminae per year from **cycle length** and **visual layer counting**, respectively. These three estimates combined lead to a composite estimate of 372 laminae deposited per year with a propagated uncertainty of 8.4 days (see Data S9). These estimates lead to the hypothesis that the laminae in *T. sanchezi* are deposited once per day.

3.4. Cyclicity in Shell Lamination

Periodicity associated with the daily laminae filtered from high-resolution proxy records (Figure 5) explains a major part of the variability within the record (Pearson's $r > 0.5$, $p < 0.01$; Figures 4 and S6 and Table 1). The residual variability in point-by-point-LA-ICP-MS profiles is characterized by ~0.6- and ~1.2-mm bundling as well as nonperiodic parameters that are likely linked to either weather events or analytical noise (Figures 4 and S5). Stacks of seasonal and daily variability show that the amplitude of daily variability varies considerably through the shell, and that the full amplitude is more faithfully captured in local point-by-point-LA-ICP-MS transects compared to LA-ICP-MS and μXRF line scans (see also Tables 1 and 2). Stacks also show that variation on a daily scale often exceeds seasonal variation (Figures 1a and 5). Variability in lamina thickness and amplitude of daily chemical cycles co-varies with annual and tidal cyclicity (Figures 1, 2, and 4; Table 1; Appendix 1, Figure A3). This visually observed annual variability in lamina thickness is only statistically significant ($p \approx 0.01$) in a weak ($R^2 = 0.15$) correlation between lamina thickness and $\delta^{13}\text{C}$, while correlation between lamina thickness and $\delta^{18}\text{O}$ is not supported by statistical evaluation (Figure 6b). In addition, a weak ontogenetic trend can also be observed, with lamina thickness increasing in the first one to two recorded growth years (or between 30 and 65 mm; Figure 1a) and stabilizing after year 2. The variability in daily lamina thickness seems to diminish with age, as is evident from decreased amplitude of variation after year 5 (~105 mm; Figure 1a). The sustained lamina thickness (and therefore daily growth rate) at later age is unusual in bivalves and reflects a common feature in rudists, of which many species are known to have sustained a “juvenile-like” rates of incrementation for many years into adulthood (Skelton, 2018).

4. Discussion

4.1. Daily Lamina Counting

The thickness of subannual laminae in *T. sanchezi* compares well with that of daily laminae in tridacnid bivalves (15–20 μm ; Sano et al., 2012; Warter et al., 2018; Warter & Müller, 2017), with laminae of approximately 50 μm for *Chione* shells (Goodwin et al., 2001) and with a daily increment width of approximately 30 μm for young specimens of *Arctica islandica* (Schöne & Giere, 2005). These comparisons are, however, tentative, since growth rates of bivalves (and therefore the thickness of increments deposited in a certain time span) can vary significantly between species or with age in the same individual (e.g., Schöne, Fiebig, et al., 2005). Identification and counting of individual daily cycles in four trace element records spanning nine growth years (**chemical layer counting**; $N = 36$) yields an average of 373 ± 12 daily laminae per year (Appendix 1). This estimate is larger than that obtained from dividing the length of the annual by that of the daily cycle, as obtained through frequency analysis ($\frac{14,800 \pm 100 \mu\text{m}}{42.7 \pm 0.34 \mu\text{m}} = 346 \pm 3.3$ days/year; **cycle length**; see section 2.8) or from counting laminae in microscopic images (**visual layer counting**; 338 ± 20 days/year; Figures 2, A3, and A13). The latter two underestimate the number of laminae per year because only 92% of the shell record was sufficiently well-preserved to enable counting of laminae (see Appendix 1). Correcting for incomplete preservation yields estimates of 376 ± 3.6 and 367 ± 22 days/year from **cycle length** and **visual layer counting**, respectively, statistically indistinguishable from the estimate based on the LA-ICP-MS record determined by line-scanning (**chemical layer counting**; see Figure 7 and section 2.8). The composite of these three estimates yields a total of 372 laminae deposited per year by *T. sanchezi*, which strongly suggests that each lamina represents one day of growth. This in turn suggests that the ~0.6- and ~1.2-mm-wide bundles are related to fortnightly (~14 days) and monthly (~28 days) tidal cycles.

It is unlikely that the daily laminae themselves are controlled by tidal influence. Instead, the clear division of the laminae into dark-light couplets suggests that the day-night cycle exerts dominant control on the formation of laminae. Similar lamination was previously observed in symbiont-bearing tridacnid bivalves which respond strongly to the daily light cycle because of their symbionts' dependence on light for photosynthesis (Warter et al., 2018; Warter & Müller, 2017). On the contrary, tide-induced shell growth, when well-developed, is expected to produce semidiurnal increments consisting of couplets of one organic-rich and one inorganic layer, resulting in two couplets per day, rather than the single couplet observed in *T. sanchezi* (e.g., Pannella, 1976; Goodwin et al., 2001). Therefore, we hypothesize that the laminae in *T. sanchezi* are paced to the solar day, rather than to tidal rhythms (semidiurnal or lunar day). This distinction is important, because even though tidal rhythms are known to produce daily growth patterns in shells of bivalves living in a variety of environments (e.g., Pannella, 1976; Schöne & Giere, 2005; Walliser et al., 2018), a subtle but significant difference exists between the length of a lunar day (presently on average 24.84 hr, or 89,424 s) and the solar day (or synodic day; presently on average 24 hr and 2.5 ms, or ~86,400 s). Grouping of laminae into fortnightly and monthly bundles likely originates from a combination of light and tidal variability.

4.2. The Earth-Moon System in the Late Cretaceous

The number of laminae per year is in close agreement with previous estimates of the number of days in a Late Cretaceous year based on independent counts of diurnal increments in various fossil taxa (Pannella, 1972: 375 days/year; Berry and Barker: 370.3 days/year) and calculations of tidal dissipation and the resulting deceleration of Earth's orbit (Laskar et al., 2004: 374.49 days/year; ocean model in Meyers & Malinverno, 2018 from Webb, 1982: ~375 days/year; Figure 7; results and explanation of estimates found in the literature are given in Appendix 1). From the number of days per year (372), we calculate that the length of a Campanian day was 8.5×10^4 s, or 23 hr and 31 min. One point-by-point-LA-ICP-MS measurement therefore represents on average 2.0×10^4 s (~5.5 hr). Based on models of the Earth-Moon system (Lowrie, 2007), the Earth-Moon distance in the Campanian calculated from the length of day obtained in this study is $3.83 \pm 0.05 \times 10^8$ m (Appendix 1), which is in agreement with established models for tidal dissipation and evolution of the Earth-Moon system over geologic time (Bills & Ray, 1999; Meyers & Malinverno, 2018). The 0.6- and 1.2-mm bundling of laminae represent ~14 and ~28 days (Figure 4), which correspond closely to the fortnightly and monthly tidal cycle, which has not changed significantly since the Campanian (Evans, 1972; Goodwin et al., 2001; Warter & Müller, 2017; Williams, 2000). Similar cyclicity was previously observed in other rudist species, most notably in the organization of cell layers in the open box-like structure of radiolithid rudists (Regidor-Higuera et al., 2007).

4.3. Implications for Paleoseasonality Reconstructions

The estimated 372 daily cycles recorded in a year leave little time for growth cessations, which are common in bivalves exposed to seasonal periods of environmental stress (Goodwin et al., 2001; Jones, 1983). Seasonal $\delta^{18}\text{O}$ fluctuations between -6‰ and -4.5‰ were previously discussed in de Winter et al. (de Winter, Goderis, et al., 2017) and could translate to an annual temperature range of $34\text{--}42\text{ °C}$ if constant sea water $\delta^{18}\text{O}$ values of -1‰ , a common value for the ice-free Cretaceous, are assumed (Shackleton, 1986). The seasonal cycle extracted from Mg/Ca, Mg/Li, and Sr/Li records in this study translates to a tentative annual temperature range of 8.6 °C , in close agreement with $\delta^{18}\text{O}$ seasonality ($\sim 9\text{ °C}$; Figure 5 and Table 1; Surge & Lohmann, 2008; Füllenbach et al., 2015; de Winter, Goderis, et al., 2017). Daily laminae deposited in the warm (low- $\delta^{18}\text{O}$, dark calcite) season are slightly thinner than average (Table 1), showing that high summer temperatures ($>40\text{ °C}$; de Winter, Goderis, et al., 2017) reduced but did not halt growth in *T. sanchezi*. Therefore, the $\delta^{18}\text{O}$ profile through the shell likely recorded the full surface water temperature seasonality, showing that Campanian tropical surface ocean temperatures exceeded those of today ($25\text{--}29\text{ °C}$; World Sea Temperatures, 2019) by over 10 °C . Warm summer temperatures (up to 35 °C) are corroborated by independent Late Cretaceous tropical sea surface temperature reconstructions based on climate modeling and chemistry of foraminifera and rudist bivalves (Pearson et al., 2001; Steuber et al., 2005). The extreme summer temperatures reconstructed from *T. sanchezi* in this study ($>40\text{ °C}$) exceed these other marine summer temperature estimates and are only matched by terrestrial summer extremes, which are generally higher than marine temperatures (Amiot et al., 2004). Such high maximum temperatures cast some doubt on the assumption that the range in $\delta^{18}\text{O}$ values can be fully attributed to temperature seasonality. Instead, even though paleogeographic reconstructions show a lack of big rivers and continents near the Samhan area (Platel et al., 1994), a decrease in the $\delta^{18}\text{O}$ value of ambient sea water in the summer season (e.g., due to an increase in local precipitation) may partly explain the negative $\delta^{18}\text{O}$ values of *T. sanchezi* calcite without the need for extreme summer temperatures. This hypothesis is corroborated by the observation that most modern bivalves are not able to extend their shell in water temperatures above $\sim 32\text{ °C}$ due to metabolic limitations (Schöne, 2008). Future research could disentangle effects of temperature and water $\delta^{18}\text{O}$ values by applying techniques that allow independent temperature reconstructions, such as clumped isotope analysis (Eiler, 2011).

4.4. Implications of Diurnal Variability in Shell Chemistry

T. sanchezi, living in a shallow marine environment (Ross & Skelton, 1993), formed tidal growth increments similar to modern shallow water tropical bivalves such as tridacnids. In tridacnid bivalves, subdaily resolved Mg/Ca and Sr/Ca variations were previously observed (Sano et al., 2012; Warter et al., 2018). While daily variability in Sr/Ca in *T. sanchezi* is similar to that measured in tridacnids ($\sim 1\text{ mmol/mol}$; Figure 5; Watanabe et al., 2004; Elliot et al., 2009), daily fluctuations in Mg/Ca far exceed those in diurnal *Tridacna* profiles (20 versus $0.4\text{--}1.4\text{ mmol/mol}$ in *Tridacna*). However, strong variability in Mg/Ca ratios between tridacnids ($3\text{--}50\text{ mmol/mol}$) may reflect vital effects in these species (Elliot et al., 2009; Gillikin et al., 2005; Watanabe et al., 2004). The difference in mineralogy between aragonitic tridacnid shells and the LMC shell of *T. sanchezi* might also explain the difference in Mg content between these taxa, as the partition constant of Mg (and other trace elements) is different for aragonite and calcite (e.g., Hasiuk & Lohmann, 2010; Lear et al., 2015; Onuma et al., 1979; Rimstidt et al., 1998). Trace element concentrations in *T. sanchezi* profiles resemble those measured in other calcitic bivalve shells (Richardson et al., 2004; Steuber, 1999; Surge & Lohmann, 2008) and daily trace element variations recorded in *T. sanchezi* exceed typical seasonal variability in these bivalves.

The high amplitude of daily relative to seasonal variability implies that light intensity and circadian rhythm exert a dominant control on shell chemistry on a daily scale. Environmental parameters dominant on the seasonal scale (e.g., sea water temperature and chemistry) play a comparatively minor role. A similar conclusion followed from daily-scale variability in lab-grown modern tridacnid bivalves (Sano et al., 2012; Warter et al., 2018). Observed diurnal variations in Mg/Ca ($10\text{--}25\text{ mmol/mol}$), Sr/Li ($100\text{--}250\text{ mol/mol}$), and Mg/Li ($1,500\text{--}2,500\text{ mol/mol}$) yield unrealistically high daily temperature ranges ($10\text{--}20\text{ °C}$; Figure 5; Surge & Lohmann, 2008; Sano et al., 2012; Montagna et al., 2014; Füllenbach et al., 2015), while diurnal temperature variations in the present-day tropical surface ocean rarely exceed 1.5 °C (Kawai & Wada, 2007). Following this rationale, temperature may explain only 15% of the daily chemical variability. Care must

be taken when applying these empirical temperature functions, since it has been demonstrated in various bivalve taxa (with aragonite as well as calcite shells) that trace element compositions are not predominantly governed by temperature (e.g., de Winter & Claeys, 2016; de Winter, Goderis, et al., 2017; Marali et al., 2017; Schöne, 2008). Instead, trace element composition is often found to relate to changes in growth rate (Gillikin et al., 2005; Lorrain et al., 2005), salinity (Klein et al., 1996), food availability (Gillikin et al., 2008), and microstructure (Foster et al., 2008; Schöne et al., 2010; Schöne et al., 2013; Shirai et al., 2014). Indeed, in modern phototrophic bivalves trace element composition is linked to changes in light availability, even at subdaily resolution (Sano et al., 2012). Similarly, the majority of diurnal trace element variability in *T. sanchezi* is likely caused by changes in light availability. Therefore, empirical temperature calibrations break down when applied on daily trace element variations. Based on the relationship between light intensity and Sr/Ca ratios in *T. sanchezi* found by Sano et al. (2012), maximum daily insolation recorded in the shell of *T. sanchezi* (531 W m^{-2}) was $\sim 100 \text{ W m}^{-2}$ higher than that recorded in modern Pacific tridacnid shells (425 W m^{-2}). The difference may be attributed to variability in water clarity, water depth, or insolation (which varies with astronomical configuration and latitude) and demonstrates the use of daily resolved insolation proxies for paleoenvironmental reconstruction. Alternatively, the fact that *T. sanchezi* built its outer shell layer from calcite rather than aragonite (as in tridacnids) may also influence the relationship between insolation and trace element content (see above). In addition, the difference in thickness between daily laminae in tridacnids ($200 \mu\text{m}$; Warter & Müller, 2017) compared to *T. sanchezi* ($\sim 40 \mu\text{m}$) may explain part of the offset, as Sr/Ca ratios in bivalves have been shown to change as a function of growth rate (Gillikin et al., 2005; Lorrain et al., 2005). Further research could focus on investigating whether the relationship between insolation and Sr/Ca ratios found by Sano et al. (2012) is applicable to other bivalve species and can be used to reliably reconstruct insolation changes. A caveat of such investigation is that all known modern photosymbiotic bivalves (subfamilies Fraginae and Tridacninae; Vermeij, 2013) produce aragonitic shells. As a result, potential relationships between Sr/Ca and insolation found in these taxa cannot be applied unconditionally to calcitic bivalves. Therefore, choosing an ideal modern analogue to aid interpretation of chemical records from taxa like *T. sanchezi* remains challenging.

4.5. Evidence for Photosymbiosis

Control of light availability on skeletal carbonate trace element composition has exclusively been demonstrated in symbiont-bearing organisms (corals (Sinclair, 2005), foraminifera (Spero et al., 2015), and bivalves (Warter et al., 2018)). The correlation has been attributed to changes in calcification rate caused by much lower activity of symbionts during low-light conditions (e.g., night; Sano et al., 2012; Carré et al., 2006). Therefore, the diurnal trace element cyclicity in *T. sanchezi* provides new evidence to support the hypothesis that *Torreites* rudists developed a mutualistic relationship with photosymbionts (Skelton & Wright, 1987; Steuber, 1999). The comparatively high $\delta^{13}\text{C}$ values ($>0\text{‰ VPDB}$) measured in *T. sanchezi* (Figure 1) are also a strong indicator of photosynthesis (McConnaughey et al., 1997). It also explains the strong seasonality in $\delta^{13}\text{C}$ in *T. sanchezi* with the highest $\delta^{13}\text{C}$ values (linked to high rates of photosynthesis) coinciding with periods of fast growth (Figure 3). The correlation between $\delta^{13}\text{C}$ and $\delta^{18}\text{O}$ values in *T. sanchezi* (Figures 3 and 6a) also supports photosymbiosis, as it was previously shown that photosynthesis can produce such a correlation (McConnaughey et al., 1997) and that this pattern is also typical for photosymbiotic bivalves such as tridacnids (McConnaughey & Gillikin, 2008).

4.6. Implications for Sclerochronology Studies

The fortnightly and monthly tidal cycles expressed in the shell of *T. sanchezi* (Figures 4, S3, and S5 and Table 1) likely reflect the effect of changes in water depth, which influenced light availability and caused stress, affecting calcification rates (Jones, 1983; Pannella, 1972; Warter et al., 2018). Aperiodic events (e.g., storms, cloud cover, and wave action) also influence light availability and growth stress and explain part of the trace element variability that is not governed by daily cycles and measurement uncertainty (Figure S5). Sampling intervals in conventional sclerochronology studies ($>0.2 \text{ mm}$) fail to detect this high-frequency variability in shell chemistry (Elliot et al., 2009; Surge & Lohmann, 2008), but tidal and diurnal variability likely explain much of the high-frequency “noise” often observed in higher-resolution ($\leq 50 \mu\text{m}$) trace element records measured in skeletal carbonates using techniques such as LA-ICP-MS and lab-based μXRF (Figure 1a; de Winter & Claeys, 2016; de Winter, Goderis, et al., 2017). These methods lack the resolution to identify daily variability in shell chemistry, but their spot

size is small enough to be affected by daily or tidal changes in trace element concentrations, which may blur the stronger seasonal cyclicity that is often the target of sclerochronology studies. Nevertheless, our data show that the presence of daily and tidal variability does not preclude the extraction of seasonality from trace element records (Figure 1), which can still be extracted using spectral analyses or growth modeling, especially in a multiproxy study that combines these records with more robust stable isotope records. The possibility to disentangle different sources of high-resolution variability in chemical records from bivalve shells paves the way for high-resolution sclerochronology studies. The temporal resolution of measurements applied in this study (5.5 hr) is not high enough to resolve individual nonperiodic events (e.g., storms). However, modern techniques allow chemical records to be measured at even higher resolution, potentially resolving such events in the future. These types of analyses would enable investigation of the frequency of extreme weather events through the year in the geological past, and yield valuable information about weather patterns in different ecosystems and climate throughout Earth's history.

5. Conclusions

The ultrahigh-resolution LA-ICP-MS analyses in this study yield the first measurements of subdaily trace element variability in Campanian rudist bivalves, and the first subdaily records of Mg/Li and Sr/Li ratios in fossil biogenic carbonate. When combined with longer, seasonally resolved multiproxy data and microscopic observations, these records allow investigation of changes in shell growth and chemistry on seasonal as well as subdaily time scales. Therefore, this approach provides a new, more accurate tool to determine the length of day in Earth's history and thus independently constrain the evolution of the Earth-Moon system over geologic time. The proposed method allows a more complete and careful discussion of the uncertainties for such estimates from bioarchives, leading to more reliable boundary conditions for astronomical models for the Earth-Moon system through geologic time. The high amplitude of daily cycles in trace element concentrations demonstrates that the light cycle exerted dominant control on calcification in *T. sanchezi*. Together with the strong seasonality observed in the $\delta^{13}\text{C}$ record, this provides strong evidence for the hypothesis that *Torreites* rudists bore photosymbionts. Given the strong influence of sunlight on calcification on the daily scale, subannually resolved chemical records from bivalve shells and other skeletal carbonates may be used as archives for reconstructing local light intensities in the geological past. In addition, these high-resolution reconstructions shed light on rapid environmental change in shallow marine tropical ecosystems during ancient greenhouse times, potentially allowing paleoclimatologists to bridge the gap from climate to weather reconstructions in the geological past. The added detail in reconstructions improves our understanding of the sensitivity of shallow marine ecosystems to environmental change and may allow the reconstruction of ancient seasonality and weather patterns. This development yields important data to confront with climate model results, improving models of greenhouse climate in the process.

6. Recommendations

However, the successful interpretation and application of such high-resolution records in terms of paleoclimate or weather patterns requires a more detailed appreciation of the mechanisms involved in the precipitation of hard tissues at the subdaily scale. Future research should therefore focus on the application of ultrahigh-resolution chemical analyses on hard tissues of modern organisms to better understand the relationship between their chemistry and environmental variables. The main focus should be on tissues that fossilize well, resist diagenetic alteration, and allow deep-time reconstructions, but should not necessarily be limited to bivalve shells. Ideally, future studies should target techniques that allow even higher sampling resolutions to be achieved, resolving chemistry at hourly or subhourly scale, to confidently resolve weather patterns or even individual tidal and storm events. Consequentially, a better understanding of trace element incorporation into hard tissues at these time scales is key, since elemental analysis techniques generally achieve higher sampling densities than stable isotope analyses due to sample size limitations. The potential relationships between trace element concentrations and insolation, growth rate, and stress are of particular interest and should be further investigated in photosymbiotic as well as asymbiotic calcifiers. Combining trace element records with better-understood proxies such as stable isotope analyses and microscopic observations in multiproxy investigation remains essential to guide the interpretation of trace element concentrations, which is still relatively uncertain. Applications of techniques that improve sampling resolution (e.g., small volume or in situ stable isotope analysis, or electron microscopy and micro/nano-CT-based

structural investigation) or facilitate interpretation (e.g., clumped isotope analysis) of these proxies should therefore be explored. Finally, application of these multiproxy investigations on older fossil material (e.g., beyond Mesozoic times) will provide an essential, reliable tool for constraining the uncertainty of length-of-day estimates and reconstructing the history of the Earth-Moon system.

Data Availability Statement

All data used for this study are available in the supporting information, which are available for download from the open-access data repository Zenodo (see de Winter et al., 2019; <https://zenodo.org/record/3477900>).

Acknowledgments

The authors would like to thank Peter Skelton and two anonymous reviewers for their helpful suggestions for improving this manuscript, as well as Ellen Thomas for additional comments and for guiding the review process as editor. We thank J. Jagt and the Natuurhistorisch Museum Maastricht for loan of the *Torreites sanchezi* shell (NHMM 2014 052). D. Verstraeten and B. Lippens (Vrije Universiteit Brussel) are thanked for technical and analytical assistance. We thank J. Vellekoop (KU Leuven) and D. de Vleeschouwer (MARUM, Bremen) for their advice on writing. Funding for this research was provided by Research Foundation Flanders (FWO, IWT700, FWOTM782, and G017217N), the FWO Hercules Foundation (HERC9, HERC24, and HERC1309), and VUB Strategic Research to P.C. A&MS-UGent acknowledges Teledyne Cetac Technologies for financial and logistic support.

References

- Al-Aasm, I. S., & Veizer, J. (1986a). Diagenetic stabilization of aragonite and low-Mg calcite, I. Trace elements in rudists. *Journal of Sedimentary Research*, 56.
- Al-Aasm, I. S., & Veizer, J. (1986b). Diagenetic stabilization of aragonite and low-Mg calcite, II. Stable isotopes in rudists. *Journal of Sedimentary Research*, 56(6), 763–770.
- Amiot, R., Lécuyer, C., Buffetaut, E., Fluteau, F., Legendre, S., & Martineau, F. (2004). Latitudinal temperature gradient during the Cretaceous Upper Campanian–Middle Maastrichtian: $\delta^{18}\text{O}$ record of continental vertebrates. *Earth and Planetary Science Letters*, 226, 255–272.
- Batenburg, S. J., Reichart, G.-J., Jilbert, T., Janse, M., Wesselingh, F. P., & Renema, W. (2011). Interannual climate variability in the Miocene: High resolution trace element and stable isotope ratios in giant clams. *Palaeogeography, Palaeoclimatology, Palaeoecology*, 306(1–2), 75–81.
- Berger, A., Loutre, M. F., & Dehant, V. (1989). Astronomical frequencies for pre-Quaternary palaeoclimate studies. *Terra Nova*, 1, 474–479.
- Bills, B. G., & Ray, R. D. (1999). Lunar orbital evolution: A synthesis of recent results. *Geophysical Research Letters*, 26, 3045–3048.
- Butler, P. G., Wanamaker, A. D. Jr., Scourse, J. D., Richardson, C. A., & Reynolds, D. J. (2013). Variability of marine climate on the North Icelandic Shelf in a 1357-year proxy archive based on growth increments in the bivalve *Arctica islandica*. *Palaeogeography, Palaeoclimatology, Palaeoecology*, 373, 141–151.
- Carré, M., Bentaleb, I., Bruguier, O., Ordinola, E., Barrett, N. T., & Fontugne, M. (2006). Calcification rate influence on trace element concentrations in aragonitic bivalve shells: Evidences and mechanisms. *Geochimica et Cosmochimica Acta*, 70(19), 4906–4920. <https://doi.org/10.1016/j.gca.2006.07.019>
- Clark, G. R. (1999). Organic matrix taphonomy in some molluscan shell microstructures. *Palaeogeography, Palaeoclimatology, Palaeoecology*, 149(1–4), 305–312.
- de Winter, N. J., & Claeys, P. (2016). Micro X-ray fluorescence (μXRF) line scanning on Cretaceous rudist bivalves: A new method for reproducible trace element profiles in bivalve calcite. *Sedimentology*, 64, 231–251. <https://doi.org/10.1111/sed.12299>
- de Winter, N. J., Goderis, S., Dehairs, F., Jagt, J. W., Fraaije, R. H., Van Malderen, S. J., et al. (2017). Tropical seasonality in the late Campanian (late Cretaceous): Comparison between multiproxy records from three bivalve taxa from Oman. *Palaeogeography, Palaeoclimatology, Palaeoecology*, 485, 740–760.
- de Winter, N. J., Goderis, S., Van Malderen, S. J. M., Sinnesael, M., Vansteenberge, S., Belza, J., et al., 2019. Supplementary Information to “Sub-daily scale chemical variability in a daily laminated *Torreites sanchezi* rudist shell: Implications for rudist paleobiology and the Cretaceous day-night cycle” to be published in *Paleoceanography and Paleoclimatology*. Zenodo Database, <https://zenodo.org/record/3477900>. Licence: CC BY 4.0.
- de Winter, N. J., Sinnesael, M., Makarona, C., Vansteenberge, S., & Claeys, P. (2017). Trace element analyses of carbonates using portable and micro-X-ray fluorescence: Performance and optimization of measurement parameters and strategies. *Journal of Analytical Atomic Spectrometry*, 32, 1211–1223.
- Eiler, J. M. (2011). Paleoclimate reconstruction using carbonate clumped isotope thermometry. *Quaternary Science Reviews*, 30(25–26), 3575–3588.
- Elliot, M., Welsh, K., Chilcott, C., McCulloch, M., Chappell, J., & Ayling, B. (2009). Profiles of trace elements and stable isotopes derived from giant long-lived *Tridacna gigas* bivalves: Potential applications in paleoclimate studies. *Palaeogeography, Palaeoclimatology, Palaeoecology*, 280, 132–142.
- Evans, J. W. (1972). Tidal growth increments in the cockle *Clinocardium nuttalli*. *Science*, 176, 416–417.
- Foster, L. C., Finch, A. A., Allison, N., Andersson, C., & Clarke, L. J. (2008). Mg in aragonitic bivalve shells: Seasonal variations and mode of incorporation in *Arctica islandica*. *Chemical Geology*, 254(1), 113–119. <https://doi.org/10.1016/j.chemgeo.2008.06.007>
- Fricke, H. C., Clyde, W. C., & O’Neil, J. R. (1998). Intra-tooth variations in $\delta^{18}\text{O}$ (PO_4) of mammalian tooth enamel as a record of seasonal variations in continental climate variables. *Geochimica et Cosmochimica Acta*, 62, 1839–1850.
- Friedman, I., O’Neil, J., & Cebula, G. (1982). Two new carbonate stable-isotope standards. *Geostandards Newsletter*, 6, 11–12. <https://doi.org/10.1111/j.1751-908X.1982.tb00340.x>
- Friedrich, O., Norris, R. D., & Erbacher, J. (2012). Evolution of middle to Late Cretaceous oceans: A 55 my record of Earth’s temperature and carbon cycle. *Geology*, 40, 107–110.
- Füllenbach, C. S., Schöne, B. R., & Mertz-Kraus, R. (2015). Strontium/lithium ratio in aragonitic shells of *Cerastoderma edule* (Bivalvia)—A new potential temperature proxy for brackish environments. *Chemical Geology*, 417, 341–355.
- Gao, Y., Ibarra, D. E., Wang, C., Caves, J. K., Chamberlain, C. P., Graham, S. A., & Wu, H. (2015). Mid-latitude terrestrial climate of East Asia linked to global climate in the Late Cretaceous. *Geology*, 43(4), 287–290.
- Gili, E., & Götz, S. (2018). Treatise Online no. 103: Part N, Volume 2, Chapter 26B: Paleocology of rudists. Treatise Online. <https://doi.org/10.17161/to.v0i0.7183>
- Gili, E., Masse, J.-P., & Skelton, P. W. (1995). Rudists as gregarious sediment-dwellers, not reef-builders, on Cretaceous carbonate platforms. *Palaeogeography, Palaeoclimatology, Palaeoecology*, 118(3), 245–267.

- Gillikin, D. P., Lorrain, A., Navez, J., Taylor, J. W., André, L., Keppens, E., et al. (2005). Strong biological controls on Sr/Ca ratios in aragonitic marine bivalve shells. *Geochemistry, Geophysics, Geosystems*, 6(5). <https://doi.org/10.1029/2004GC000874>
- Gillikin, D. P., Lorrain, A., Paulet, Y.-M., André, L., & Dehairs, F. (2008). Synchronous barium peaks in high-resolution profiles of calcite and aragonite marine bivalve shells. *Geo-Marine Letters*, 28(5–6), 351–358.
- Goodwin, D. H., Flessa, K. W., Schone, B. R., & Dettman, D. L. (2001). Cross-calibration of daily growth increments, stable isotope variation, and temperature in the Gulf of California bivalve mollusk *Chione cortezi*: Implications for paleoenvironmental analysis. *Palaios*, 16, 387–398.
- Gothmann, A. M., Stolarski, J., Adkins, J. F., Schoene, B., Dennis, K. J., Schrag, D. P., et al. (2015). Fossil corals as an archive of secular variations in seawater chemistry since the Mesozoic. *Geochimica et Cosmochimica Acta*, 160, 188–208.
- Gradstein, F. M., Ogg, J. G., Schmitz, M., & Ogg, G. (2012). *The geologic time scale 2012*. Kidlington, UK: Elsevier.
- Hasiuk, F. J., & Lohmann, K. C. (2010). Application of calcite Mg partitioning functions to the reconstruction of paleocean Mg/Ca. *Geochimica et Cosmochimica Acta*, 74(23), 6751–6763. <https://doi.org/10.1016/j.gca.2010.07.030>
- Huber, B. T., Norris, R. D., & MacLeod, K. G. (2002). Deep-sea paleotemperature record of extreme warmth during the Cretaceous. *Geology*, 30, 123–126.
- Huck, S., & Heimhofer, U. (2015). Improving shallow-water carbonate chemostratigraphy by means of rudist bivalve sclerochemistry. *Geochemistry, Geophysics, Geosystems*, 16(9), 3111–3128.
- Huybers, P., & Curry, W. (2006). Links between annual, Milankovitch and continuum temperature variability. *Nature*, 441, 329.
- Jones, D. S. (1983). Sclerochronology: reading the record of the molluscan shell: Annual growth increments in the shells of bivalve molluscs record marine climatic changes and reveal surprising longevity. *American Scientist*, 71, 384–391.
- Judd, E. J., Wilkinson, B. H., & Ivany, L. C. (2018). The life and time of clams: Derivation of intra-annual growth rates from high-resolution oxygen isotope profiles. *Palaeogeography, Palaeoclimatology, Palaeoecology*, 490, 70–83.
- Kawai, Y., & Wada, A. (2007). Diurnal sea surface temperature variation and its impact on the atmosphere and ocean: A review. *J Oceanogr*, 63, 721–744. <https://doi.org/10.1007/s10872-007-0063-0>
- Kennedy, W. J., Jagt, J. W. M., Hanna, S. S., & Schulp, A. S. (2000). Late Campanian ammonites from the Saiwan area (Huqf Desert, Sultanate of Oman). *Cretaceous Research*, 21(4), 553–562. <https://doi.org/10.1006/cres.2000.0217>
- Klein, R. T., Lohmann, K. C., & Thayer, C. W. (1996). Sr/Ca and $^{13}\text{C}/^{12}\text{C}$ ratios in skeletal calcite of *Mytilus trossulus*: Covariation with metabolic rate, salinity, and carbon isotopic composition of seawater. *Geochimica et Cosmochimica Acta*, 60(21), 4207–4221. [https://doi.org/10.1016/S0016-7037\(96\)00232-3](https://doi.org/10.1016/S0016-7037(96)00232-3)
- Laskar, J., Robutel, P., Joutel, F., Gastineau, M., Correia, A. C. M., & Levrard, B. (2004). A long-term numerical solution for the insolation quantities of the Earth. *Astronomy and Astrophysics*, 428(1), 261–285. <https://doi.org/10.1051/0004-6361:20041335>
- Lear, C. H., Coxall, H. K., Foster, G. L., Lunt, D. J., Mawbey, E. M., Rosenthal, Y., et al. (2015). Neogene ice volume and ocean temperatures: Insights from infaunal foraminiferal Mg/Ca paleothermometry. *Paleoceanography*, 30(11), 1437–1454.
- Lorrain, A., Gillikin, D. P., Paulet, Y.-M., Chauvaud, L., Le Mercier, A., Navez, J., & André, L. (2005). Strong kinetic effects on Sr/Ca ratios in the calcitic bivalve *Pecten maximus*. *Geology*, 33(12), 965–968.
- Lowrie, W. (2007). *Fundamentals of Geophysics, 2nd 200 Edition*, (p. 415). Cambridge, UK: Cambridge University Press.
- Marali, S., Schöne, B. R., Mertz-Kraus, R., Griffin, S. M., Wanamaker, A. D., Butler, P. G., et al. (2017). Reproducibility of trace element time-series (Na/Ca, Mg/Ca, Mn/Ca, Sr/Ca, and Ba/Ca) within and between specimens of the bivalve *Arctica islandica*: A LA-ICP-MS line scan study. *Palaeogeography, Palaeoclimatology, Palaeoecology*, 484, 109–128. <https://doi.org/10.1016/j.palaeo.2016.11.024>
- McConnaughey, T. (1989). ^{13}C and ^{18}O isotopic disequilibrium in biological carbonates: II. In vitro simulation of kinetic isotope effects. *Geochimica et Cosmochimica Acta*, 53(1), 163–171.
- McConnaughey, T. A., Burdett, J., Whelan, J. F., & Paull, C. K. (1997). Carbon isotopes in biological carbonates: Respiration and photosynthesis. *Geochimica et Cosmochimica Acta*, 61, 611–622.
- McConnaughey, T. A., & Gillikin, D. P. (2008). Carbon isotopes in mollusk shell carbonates. *Geo-Marine Letters*, 28(5–6), 287–299.
- Meehl, G. A., Stocker, T. F., Collins, W. D., Friedlingstein, P., Gaye, T., Gregory, J. M., et al., 2007. Global climate projections. In: IPCC, 2007: Climate Change 2007: The physical science basis. contribution of Working Group I to the Fourth Assessment Report of the Intergovernmental Panel on Climate Change, Cambridge University Press, UK.
- Meyers, S. R., 2014. Astrochron: An R package for astrochronology. Available at cran.rproject.org/web/packages/astrochron/index.html.
- Meyers, S. R., & Malinverno, A. (2018). Proterozoic Milankovitch cycles and the history of the solar system. *Proceedings of the National Academy of Science*, 201717689. <https://doi.org/10.1073/pnas.1717689115>
- Montagna, P., McCulloch, M., Douville, E., López Correa, M., Trotter, J., Rodolfo-Metalpa, R., et al. (2014). Li/Mg systematics in scleractinian corals: Calibration of the thermometer. *Geochimica et Cosmochimica Acta*, 132, 288–310. <https://doi.org/10.1016/j.gca.2014.02.005>
- Onuma, N., Masuda, F., Hirano, M., & Wada, K. (1979). Crystal structure control on trace element partition in molluscan shell formation. *Geochemical Journal*, 13(4), 187–189.
- Pannella, G. (1972). Paleontological evidence on the Earth's rotational history since early Precambrian. *Astrophysics and Space Science*, 16, 212–237.
- Pannella, G. (1976). Tidal growth patterns in recent and fossil mollusc bivalve shells: A tool for the reconstruction of paleotides. *Naturwissenschaften*, 63(12), 539–543.
- Pearson, P. N., Ditchfield, P. W., Singano, J., Harcourt-Brown, K. G., Nicholas, C. J., Olsson, R. K., et al. (2001). Warm tropical sea surface temperatures in the Late Cretaceous and Eocene epochs. *Nature*, 413, 481.
- Philip, J. M., & Platel, J.-P. (1995). Stratigraphy and rudist biozonation of the Campanian and the Maastrichtian of Eastern Oman. *Revista mexicana de ciencias geológicas*, 12, 15.
- Platel, J. P., Philip, J., Bourdillon-de-Grissac, C., Babinot, J. F., Roger, J., & Mercadier, C. (1994). Modalités de la transgression campanienne sur le massif du Haushi-Huqf (Oman); stratigraphie, contexte géodynamique et paléoenvironnements. *Bulletin de la Société Géologique de France*, 165, 147–161.
- Price, G. D., Twitchett, R. J., Wheelley, J. R., & Buono, G. (2013). Isotopic evidence for long term warmth in the Mesozoic. *Scientific Reports*, 3, 1438.
- R Development Core Team, R (2008). *R: A language and environment for statistical computing*. Austria: R foundation for statistical computing Vienna.

- Regidor-Higuera, I., García-Garmilla, F., & Skelton, P. W. (2007). Sclerochronology and diagenesis of Late Cretaceous radiolitids (Bivalvia, Hippuritoida), Spain. In *Cretaceous Rudists and Carbonate Platforms: Environmental Feedback*, (Vol. 87, pp. 115–140). SEPM Society for Sedimentary Geology, Tulsa (OK), USA: SEPM Special Publication.
- Richardson, C. A., Peharda, M., Kennedy, H., Kennedy, P., & Onofri, V. (2004). Age, growth rate and season of recruitment of *Pinna nobilis* (L) in the Croatian Adriatic determined from Mg:Ca and Sr:Ca shell profiles. *Journal of Experimental Marine Biology and Ecology*, 299, 1–16.
- Rimstidt, J. D., Balog, A., & Webb, J. (1998). Distribution of trace elements between carbonate minerals and aqueous solutions. *Geochimica et Cosmochimica Acta*, 62(11), 1851–1863.
- Ross, D. J., Skelton, P. W., 1993. Rudist formations of the Cretaceous: A palaeoecological, sedimentological and stratigraphical review. *Sedimentology review*/1 73–91.
- Sano, Y., Kobayashi, S., Shirai, K., Takahata, N., Matsumoto, K., Watanabe, T., et al. (2012). Past daily light cycle recorded in the strontium/calcium ratios of giant clam shells. *Nature Communications*, 3, 761.
- Schöne, B. R. (2008). The curse of physiology: Challenges and opportunities in the interpretation of geochemical data from mollusk shells. *Geo-Marine Letters*, 28(5–6), 269–285.
- Schöne, B. R., Fiebig, J., Pfeiffer, M., Gleß, R., Hickson, J., Johnson, A. L., et al. (2005). Climate records from a bivalved Methuselah (*Arctica islandica*, Mollusca; Iceland). *Palaeogeography, Palaeoclimatology, Palaeoecology*, 228, 130–148.
- Schöne, B. R., & Giere, O. (2005). Growth increments and stable isotope variation in shells of the deep-sea hydrothermal vent bivalve mollusk *Bathymodiolus brevior* from the North Fiji Basin, Pacific Ocean. *Deep Sea Research Part I: Oceanographic Research Papers*, 52(10), 1896–1910.
- Schöne, B. R., Radermacher, P., Zhang, Z., & Jacob, D. E. (2013). Crystal fabrics and element impurities (Sr/Ca, Mg/Ca, and Ba/Ca) in shells of *Arctica islandica*: Implications for paleoclimate reconstructions. *Palaeogeography, Palaeoclimatology, Palaeoecology*, 373, 50–59.
- Schöne, B. R., Zhang, Z., Jacob, D., Gillikin, D. P., Tütken, T., Garbe-Schönberg, D., et al. (2010). Effect of organic matrices on the determination of the trace element chemistry (Mg, Sr, Mg/Ca, Sr/Ca) of aragonitic bivalve shells (*Arctica islandica*): Comparison of ICP-OES and LA-ICP-MS data. *Geochemical Journal*, 44(1), 23–37.
- Schöne, B. R., Zhang, Z., Radermacher, P., Thébault, J., Jacob, D. E., Nunn, E. V., & Maurer, A.-F. (2011). Sr/Ca and Mg/Ca ratios of ontogenetically old, long-lived bivalve shells (*Arctica islandica*) and their function as paleotemperature proxies. *Palaeogeography, Palaeoclimatology, Palaeoecology*, 302, 52–64.
- Schumann, P. D. D. (1995). Upper cretaceous rudist and stromatopod associations of central Oman (Arabian Peninsula). *Facies*, 32(1), 189–202. <https://doi.org/10.1007/BF02536868>
- Seilacher, A. (1998). Rudists as bivalvian dinosaurs. In P. A. Johnston, & J. W. Haggart (Eds.), *Bivalves: An eon of evolution—Paleontological studies honoring Norman D. Newell*, (pp. 423–436). Calgary: University of Calgary Press.
- Shackleton, N. J. (1986). Paleogene stable isotope events. *Palaeogeography, Palaeoclimatology, Palaeoecology*, 57(1), 91–102.
- Shirai, K., Schöne, B. R., Miyaji, T., Radermacher, P., Krause, R. A., & Tanabe, K. (2014). Assessment of the mechanism of elemental incorporation into bivalve shells (*Arctica islandica*) based on elemental distribution at the microstructural scale. *Geochimica et Cosmochimica Acta*, 126, 307–320.
- Sinclair, D. J. (2005). Correlated trace element “vital effects” in tropical corals: A new geochemical tool for probing biomineralization. *Geochimica et Cosmochimica Acta*, 69, 3265–3284. <https://doi.org/10.1016/j.gca.2005.02.030>
- Skelton, P. W. (2018). Introduction to the Hippuritida (rudists): Shell structure, anatomy, and evolution. Treatise Online 104 Part N, Volume 1. Chapter, 26A, 1–37.
- Skelton, P. W., & Wright, V. P. (1987). A Caribbean rudist bivalve in Oman-island-hopping across the Pacific in the Late Cretaceous. *Palaeontology*, 30, 505–529.
- Spero, H. J., Eggins, S. M., Russell, A. D., Vetter, L., Kilburn, M. R., & Hönisch, B. (2015). Timing and mechanism for intratest Mg/Ca variability in a living planktic foraminifer. *Earth and Planetary Science Letters*, 409, 32–42.
- Steuber, T. (1996). Stable isotope sclerochronology of rudist bivalves: Growth rates and Late Cretaceous seasonality. *Geology*, 24, 315–318.
- Steuber, T. (1999). Isotopic and chemical intra-shell variations in low-Mg calcite of rudist bivalves (Mollusca-Hippuritacea): Disequilibrium fractionations and late Cretaceous seasonality. *International Journal of Earth Sciences*, 88, 551–570.
- Steuber, T., Mitchell, S. F., Buhl, D., Gunter, G., & Kasper, H. U. (2002). Catastrophic extinction of Caribbean rudist bivalves at the Cretaceous-Tertiary boundary. *Geology*, 30(11), 999–1002.
- Steuber, T., Rauch, M., Masse, J.-P., Graaf, J., & Malkoč, M. (2005). Low-latitude seasonality of Cretaceous temperatures in warm and cold episodes. *Nature*, 437, 1341.
- Surge, D., & Lohmann, K. C. (2008). Evaluating Mg/Ca ratios as a temperature proxy in the estuarine oyster. *Crassostrea virginica*. *Journal of Geophysical Research: Biogeosciences*, 113.
- Thomson, D. J. (1982). Spectrum estimation and harmonic analysis. *Proceedings of the IEEE*, 70(9), 1055–1096.
- Veizer, J., & Prokoph, A. (2015). Temperatures and oxygen isotopic composition of Phanerozoic oceans. *Earth-Science Reviews*, 146, 92–104. <https://doi.org/10.1016/j.earscirev.2015.03.008>
- Vermeij, G. J. (2013). The evolution of molluscan photosymbioses: A critical appraisal. *Biological Journal of the Linnean Society*, 109(3), 497–511.
- Vogel, K. (1975). Endosymbiotic algae in rudists? *Palaeogeography, Palaeoclimatology, Palaeoecology*, 17(4), 327–332. [https://doi.org/10.1016/0031-0182\(75\)90005-X](https://doi.org/10.1016/0031-0182(75)90005-X)
- Walliser, E. O., Mertz-Kraus, R., & Schöne, B. R. (2018). The giant inoceramid *Platyceramus platinus* as a high-resolution paleoclimate archive for the Late Cretaceous of the Western Interior Seaway. *Cretaceous Research*, 86, 73–90. <https://doi.org/10.1016/j.cretres.2018.01.010>
- Warter, V., Erez, J., & Müller, W. (2018). Environmental and physiological controls on daily trace element incorporation in *Tridacna crocea* from combined laboratory culturing and ultra-high resolution LA-ICP-MS analysis. *Palaeogeography, Palaeoclimatology, Palaeoecology*, 496, 32–47. <https://doi.org/10.1016/j.palaeo.2017.12.038>
- Warter, V., & Müller, W. (2017). Daily growth and tidal rhythms in Miocene and modern giant clams revealed via ultra-high resolution LA-ICPMS analysis—A novel methodological approach towards improved sclerochemistry. *Palaeogeography, Palaeoclimatology, Palaeoecology*, 465, 362–375.
- Watanabe, T., Suzuki, A., Kawahata, H., Kan, H., & Ogawa, S. (2004). A 60-year isotopic record from a mid-Holocene fossil giant clam (*Tridacna gigas*) in the Ryukyu Islands: Physiological and paleoclimatic implications. *Palaeogeography, Palaeoclimatology, Palaeoecology*, 212, 343–354.
- Weiner, S., & Dove, P. M. (2003). An overview of biomineralization processes and the problem of the vital effect. *Reviews in mineralogy and geochemistry*, 54, 1–29.

- Williams, G. E. (2000). Geological constraints on the Precambrian history of Earth's rotation and the Moon's orbit. *Rev. Geophys.*, 38, 37–59. <https://doi.org/10.1029/1999RG900016>
- World Sea Temperatures Ltd, C.G.S.T.-A.-C. (2019). Şalālah Water Temperature|Oman|Sea Temperatures [WWW Document]. World Sea Temperatures. URL <http://www.seatemperature.org/middle-east/oman/allah.htm>
- Yonge, C. M. (1936). Mode of life, feeding, digestion and symbiosis with zooxanthellae in the Tridacnidae. Great Barrier Reef Expedition 1928–29. *Scientific Reports*, 1, 283–321.
- Zachos, J., Pagani, M., Sloan, L., Thomas, E., & Billups, K. (2001). Trends, rhythms, and aberrations in global climate 65 Ma to present. *Science*, 292, 686–693.